Modeling and design of bidirectional pendulum tuned mass dampers using axial or tangential homogeneous friction damping

Modeling and design of bidirectional pendulum tuned mass dampers using axial or tangential homogeneous friction damping

Emiliano Matta

Politecnico di Torino, Corso Duca degli Abruzzi 24, 10129 Turin, Italy
E-mail: emiliano.matta@polito.it · Phone: +39 011 090 4867 · ORCID: 0000-0001-5453-1470

Abstract
As a development of the classical pendulum vibration absorber, bidirectional pendulum TMDs (BTMDs) have been recently proposed, capable to resonate with the main structure along both its horizontal directions by virtue of their optimally designed three-dimensional (3D) pendulum surface. To provide BTMDs with the required energy dissipation capability, two damping mechanisms based on respectively axial and tangential friction were invented as an alternative to ordinary viscous dashpots. The first one consists of a vertical axial-friction damper connecting the BTMD to the main structure. The second one consists of a tangential friction spatially variable along the pendulum surface in proportion to the modulus of the surface gradient vector. Both mechanisms are fundamentally characterized by a nonlinear but homogeneous first-order model which makes their effectiveness independent from the excitation level. This paper compares the two friction paradigms with the classical viscous one. To this purpose, first a unifying fully nonlinear 3D model is established through Lagrangian mechanics, then an optimal design method is proposed, based on either H_∞ or H_2 norm minimization criteria. Extensive numerical simulations are performed to show the pros and cons of the three damping options and of the two optimization approaches. Results demonstrate that the three types exhibit a similar performance against unidirectional excitation but that the axial-friction type loses most of its effectiveness under bidirectional excitation whenever the pendulum surface is axial- or nearly axial-symmetrical, because of the insurgence of a peculiar rotational motion which virtually deactivates the friction damper. Results also show that the H_∞ design criterion is more robust than the H_2 design criterion, and that both criteria outperform previous simplified approaches proposed in the literature. It is concluded that, once properly designed and until stroke demand does not exceed their intrinsic stroke limitations, BTMDs are an effective vibration control strategy, which can be implemented through a variety of damping options, and that the two homogeneous friction mechanisms, and particularly the tangential one, are promising paradigms to provide amplitude-independent damping to engineering pendular systems.

Keywords: structural vibration control; tuned mass dampers; bidirectional pendulum systems; Lagrangian mechanics; homogeneous friction damping; wind mitigation.

1 Introduction

Passive tuned mass dampers (TMDs) are a mature strategy of structural vibration control, widely applied in civil and mechanical engineering [1]. The most elementary scheme of a TMD consists of a single-degree-of-freedom (SDOF) linear oscillator attached to the main structure, capable of absorbing and dissipating vibratory energy from one structural target mode through frequency tuning and damping optimization. According whether their restoring force is elastic or gravitational, TMDs are mainly classified in the translational and pendulum categories, and the pendulum category is further distinguished into the "supported" and the "hanging" pendulum types, depending whether the mass of the absorber is constrained to move along a physical curved recess or suspended through ropes or bars. In the last decade, supported pendulum TMDs have increasingly attracted the attention of the research community, because of their compactness, durability and versatility of shape. They include a variety of configurations, such as the ball pendulum [2,3], the rolling and sliding pendulums (with single or double concavity) [4,5] and the rocking pendulum. In [6] a novel rolling ball damper is proposed for controlling wind turbines, made of multiple steel balls rolling in a spherical concavity and dissipating through rolling friction and impact. In [7] a novel unbalanced rolling pendulum TMD is presented, where the gravitational restoring force is

produced by the unbalanced distribution of mass within the rolling body. In [8] a track nonlinear energy sink (NES) is proposed, whose specially shaped, smooth and symmetric track profile provides the desired essentially nonlinear restoring force which is typical of NESs. In [9] an asymmetrical variant of the said track NES is introduced, in which the smooth track nonlinearity combines with a discontinuous impact nonlinearity. In [10] an interesting application is presented of a rolling ball pendulum embedded in hollow slabs of civil structures.

As an alternative to the pendulum schemes listed above, which are all either two-dimensional (2D) (i.e. constrained along a planar vertical profile) or three-dimensional (3D) but axial-symmetrical (i.e. constrained along a surface of revolution), bidirectional pendulum TMDs (BTMDs) have also been proposed which can be tuned to the main structure along both horizontal directions even when the corresponding structural target frequencies are different, by virtue of an optimally designed (generally non-axial-symmetrical) 3D pendulum surface. This concept has been implemented in two main variants, respectively belonging to the supported and to the hanging pendulum types. The first variant is the rolling-pendulum BTMD introduced in [11]. In this case, the 3D pendulum surface is realized by a special 3D rolling-pendulum bearing, made of two identical concavities symmetrically facing each other and sandwiching a rolling ball. By varying the shape of the two concavities and the radius of the rolling ball, any 3D surface can be obtained. The second variant is the hanging-pendulum BTMD proposed in [12]. In this case, the 3D pendulum surface is realized by a special Y-shaped arrangement of the suspending cables. By varying the length of the vertical cable and/or of the inclined cables, any toroidal surface can be obtained.

In these two variants of BTMDs, energy dissipation is produced either by classical horizontal viscous dampers [11] or by an original arrangement of a vertical axial-friction damper [12]. A third damping option has been very recently proposed for supported BTMDs by the same author, consisting of a tangential rolling- or sliding-friction spatially variable along the pendulum surface in proportion to the modulus of the surface gradient vector [13]. Both the axial-friction and the tangential-friction mechanisms mentioned above are fundamentally characterized by a nonlinear but homogeneous first-order model. Therefore, in the small-displacement domain both friction types ensure the BTMD an equivalent damping ratio and an effectiveness which are independent from the amplitude of motion [14], contrary to what happens when a constant friction acts in the direction of motion of the absorber, in which case the equivalent damping ratio becomes inversely proportional to the amplitude and the effectiveness becomes amplitude-dependent [15,10].

Focusing on bidirectional pendulum TMDs of the supported type, this paper compares the two friction paradigms, respectively called the homogeneous-axial BTMD (HA-BTMD) and the homogeneous-tangential BTMD (HT-BTMD) and jointly denoted as the homogeneous BTMD (H-BTMD), with the classical viscous paradigm, here named the viscous BTMD (V-BTMD). To this purpose, first a unifying fully nonlinear 3D BTMD model is derived through Lagrangian mechanics, then an optimal design methodology is proposed. Extensive numerical simulations of the optimally designed devices mounted on SDOF and multi-degree-of-freedom (MDOF) structures are finally performed under stationary force input, revealing the respective pros and cons of the three damping options. Main contributions of this paper are as follows: (i) establishing a common modelling framework, representative of all three existing BTMD types, by combining contributions from previous studies; (ii) presenting a common BTMD design procedure, rigorously valid for SDOF linear structures under low-amplitude harmonic or white-noise force excitations but extendable to more general cases, whose main novelty resides in the solution, never attempted before for H-BTMDs, of an H_∞ or H_2 norm minimization, here numerically performed for various design scenarios; (iii) showing the superior robustness of the H_∞ optimal solution over the H_2 optimal solution, and the greater effectiveness of both solutions over existing simplified optimization criteria; (iv) evaluating the optimal BTMDs in a variety of cases, for different structural features and excitation levels; (v) proving, both analytically and numerically, the superior 3D performance of the HT-BTMD over the HA-BTMD, this latter exhibiting, in axial- or nearly axial-symmetrical cases, a peculiar (so far undocumented), insufficiently-damped rotational mode which drastically reduces its mitigation

capabilities; (vi) showing, on the other hand, the substantial equivalence of the V-BTMD and of the HT-BTMD in a variety of design situations.
The remaining of this paper is organized as follows: in Section 2 the fully nonlinear 3D model of a BTMD of either viscous, axial-friction or tangential-friction damping types is derived; in Section 3 an optimal design method is presented for the three types; in Section 4 the three alternatives are compared in the small-displacement domain; in Section 5 the three alternatives are compared in the large-displacement domain; in Section 6 a case study is illustrated; in Section 7 conclusions are drawn.

2. The BTMD unifying analytical model

This section establishes the fully nonlinear 3D model of a BTMD accounting for: (i) one or more viscous dampers connecting it to the supporting structure; (ii) an axial-friction damper connecting it to the supporting structure; (iii) a variable tangential friction acting along the pendulum surface; and (iv) a fail-safe bumper connecting it to the supporting structure. The general modelling framework, based on Lagrangian holonomic mechanics, is the one already used by other authors in [12] and by the same author in [13]. However, no tangential friction is considered in [12] and no axial friction in [13]. Also, the fail-safe bumper is here modelled as in [13] rather than in [12]. This framework differs from the one, based on Appell's non-holonomic dynamics, adopted in [11], specifically accounting for the rotational motion of the rolling sphere, here instead neglected. By merging contributions from [12] and [13], this section proposes a unifying model simultaneously representing all possible dissipation mechanisms currently available for BTMD applications.

2.1 The pendulum kinematics

The BTMD model is schematized in Figure 1. It consists of a point mass m subject to gravity g and constrained to move along a generic 3D differentiable concave-up surface. The surface is minimum in O, where it is rigidly connected to the structural support. The BTMD rotational inertia is neglected for simplicity. The motion of m along the surface is opposed by four possible mechanisms, namely: (i) the viscous damper connecting m to the support in A; (ii) the vertical axial-friction damper connecting m to the structure in B; (iii) the tangential friction acting along the surface; and (iv) the fail-safe bumper connecting m to the support in C. Because the rotations of the structural support are assumed negligible, the surface as well as points A, B and C purely translate together with the support in O.
Denoting by u, v and w the coordinates of m with respect to the local reference system xyz fixed to the support in O, the pendulum kinematic constraint is defined by the surface equation $w = w(u,v) = w(\mathbf{q})$, and the relative displacement of m (w.r.t. its support) is given by $\mathbf{r} = [u, v, w]^T = [\mathbf{q}^T, w(\mathbf{q})]^T$, where u and v are the two independent coordinates, w is the dependent coordinate and $\mathbf{q} = [u, v]^T$ is the absorber degree-of-freedom vector. For simplicity, x and y are taken parallel to the two structural target modeshapes, assumed mutually orthogonal in plan. The versors associated with x, y and z are $\hat{\mathbf{i}}$, $\hat{\mathbf{j}}$ and $\hat{\mathbf{k}}$. The absolute acceleration of the structural support is $\boldsymbol{a} = [a_x, a_y, a_z]^T = [\boldsymbol{a}_h{}^T, a_z]^T$ and the relative velocity of m is $\dot{\mathbf{r}} = \frac{\partial \mathbf{r}}{\partial \mathbf{q}}\dot{\mathbf{q}} = \mathbf{J}\dot{\mathbf{q}}$, where $\mathbf{J} = \frac{\partial \mathbf{r}}{\partial \mathbf{q}} = \left[\frac{\partial \mathbf{r}}{\partial u} \quad \frac{\partial \mathbf{r}}{\partial v}\right] = [\mathbf{I}, \nabla w]^T$ is the Jacobian matrix of the kinematic transformation and $\nabla w = \frac{\partial w}{\partial \mathbf{q}}$ is the surface gradient vector.

2.2 The details of the dissipative mechanisms

Four dissipative mechanisms are included in the model. The first three mechanisms, i.e. viscous damping, axial friction and tangential friction, although assumed mutually exclusive in the following sections, are here modelled together. The fourth mechanism, i.e. the fail-safe bumper, introduced to prevent excessive BTMD strokes, is always present but operates only in the large-displacement domain. For brevity, only one viscous damper (arbitrarily oriented) is supposed in deriving the model, despite multiple viscous dampers are generally admitted and at least two are indeed required if both target modes need mitigation. The four said mechanisms are modelled as follows.

2.2.1 Viscous damping

As shown in Figure 1, the viscous damper has damping coefficient c, undeformed length l_{c0} and deformed length l_c. Denoting by $\hat{\mathbf{c}}_0$ and $\hat{\mathbf{c}}$ respectively the undeformed and deformed versors coaxial with the damper (oriented from A to m), its undeformed and deformed position vectors are respectively $\mathbf{l}_{c0} = l_{c0}\hat{\mathbf{c}}_0$ and $\mathbf{l}_c = l_c\hat{\mathbf{c}} = \mathbf{l}_{c0} + \mathbf{r}$, and the damper axial elongation is $s_c = l_c - l_{c0}$. Its axial elongation rate is then $\dot{s}_c = \left(\frac{\partial s_c}{\partial \mathbf{q}}\right)^T \dot{\mathbf{q}}$ or equivalently $\dot{s}_c = \hat{\mathbf{c}}^T\dot{\mathbf{r}} = \hat{\mathbf{c}}^T\mathbf{J}\dot{\mathbf{q}}$, this latter expression representing the projection of $\dot{\mathbf{r}}$ on $\hat{\mathbf{c}}$. Denoting as $f_c = c\dot{s}_c$ the axial force in the damper, $\mathbf{f}_c = -f_c\hat{\mathbf{c}}$ is the viscous force vector acting on m.

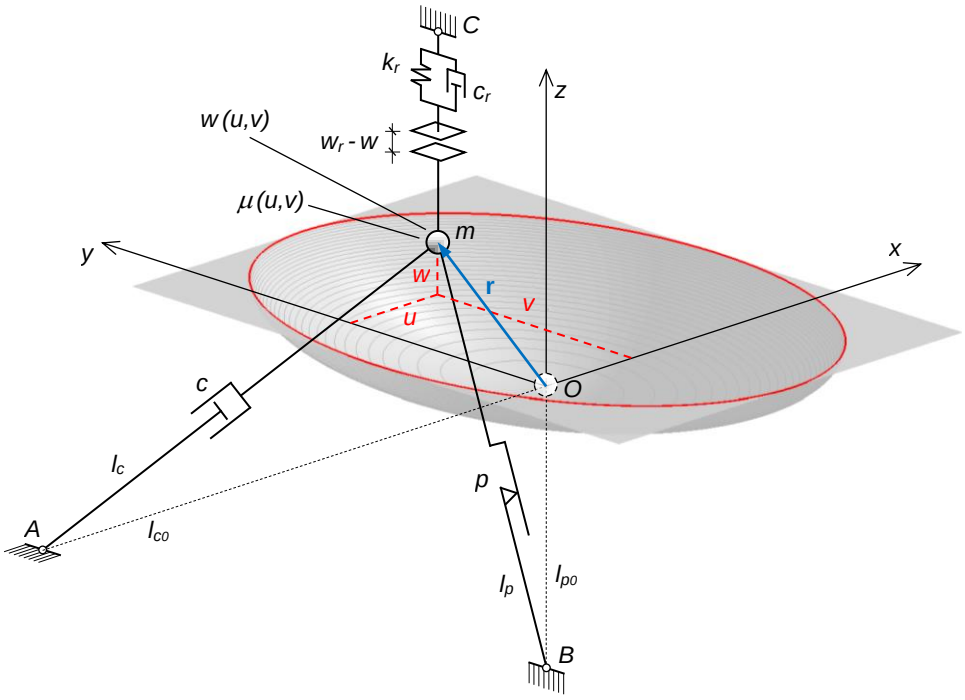

Figure 1. Schematic axonometric view of the BTMD in its deformed position.

2.2.2 Axial friction

As shown in Figure 1, the friction damper has slip force p, undeformed length l_{p0} and deformed length l_p. For simplicity, a rigid-plastic (dry) friction model is adopted. Admitting for now that the friction damper might be arbitrarily oriented, and denoting by $\hat{\mathbf{p}}_0$ and $\hat{\mathbf{p}}$ its undeformed and deformed coaxial versors (oriented from B to m), its undeformed and deformed position vectors are $\mathbf{l}_{p0} = l_{p0}\hat{\mathbf{p}}_0$ and $\mathbf{l}_p = l_p\hat{\mathbf{p}} = \mathbf{l}_{p0} + \mathbf{p}$, and its axial elongation is $s_p = l_p - l_{p0}$. Its axial elongation rate is then $\dot{s}_p = \left(\frac{\partial s_p}{\partial \mathbf{q}}\right)^T \dot{\mathbf{q}}$ or equivalently $\dot{s}_p = \hat{\mathbf{p}}^T\dot{\mathbf{r}} = \hat{\mathbf{p}}^T\mathbf{J}\dot{\mathbf{q}}$. Denoting as $f_p = \text{sign}(\dot{s}_p)\, p$ the axial force in the damper, $\mathbf{f}_p = -f_p\hat{\mathbf{p}}$t is the axial-friction force vector acting on m.

2.2.3 Tangential friction

As schematized in Figure 1, the 3D pendulum surface presents a tangential-friction coefficient spatially varying as $\mu = \mu(u, v) = \mu(\mathbf{q})$. For simplicity, an isotropic rigid-plastic friction model is assumed, with equal static and kinetic friction coefficients. The tangential-friction force value is:

$$f_\mu = \mu(\mathbf{q})N \tag{1}$$

and the tangential-friction force vector acting on m is $\mathbf{f}_\mu = -f_\mu \hat{\mathbf{t}}$, where N is the modulus of the normal reaction force vector $\mathbf{N}$ at the contact point and $\hat{\mathbf{t}}$ is the tangent versor, given by $\hat{\mathbf{t}} = \mathbf{0}$ if $\dot{\mathbf{r}} = \mathbf{0}$ and by $\hat{\mathbf{t}} = \dot{\mathbf{r}}/\|\dot{\mathbf{r}}\| = \mathbf{J}\dot{\mathbf{q}}/\sqrt{\dot{\mathbf{q}}^T\mathbf{J}^T\mathbf{J}\dot{\mathbf{q}}}$ if $\dot{\mathbf{r}} \neq \mathbf{0}$.
Although the unifying model now under construction accepts in principle any friction pattern, here the attention is focused on the friction law recently proposed in [13], defined by:

$$\mu(\mathbf{q}) = \|\boldsymbol{\mu}_\mathbf{0} \nabla w\| \tag{2}$$

which describes a friction coefficient varying along the surface as the modulus of the surface gradient vector ∇w pre-multiplied by the diagonal friction matrix:

$$\boldsymbol{\mu}_\mathbf{0} = \begin{bmatrix} \mu_{0x} & 0 \\ 0 & \mu_{0y} \end{bmatrix} \tag{3}$$

where μ_{0x} and μ_{0y} are the tangential-friction damping ratios along x and y. If $\mu_{0x} = \mu_{0y} = \mu_0$, the friction matrix becomes $\boldsymbol{\mu}_\mathbf{0} = \mu_0 \mathbf{I}$ and Eq. (2) becomes:

$$\mu(\mathbf{q}) = \mu_0 \|\nabla w\| \tag{4}$$

which indeed describes a friction coefficient proportional to the modulus of the surface gradient vector. As show in [13], for a tangential-friction BTMD obeying Eq. (2), necessary and sufficient condition for the re-centring of the absorber is that $\max(\mu_{0x}, \mu_{0y}) < 1$. This condition becomes $\mu_0 < 1$ if $\mu_{0x} = \mu_{0y} = \mu_0$.

2.2.4 Viscoelastic bumping

As shown in Figure 1, the bumper has stiffness k_r, damping coefficient c_r and initial clearance w_r. The bumper reacts along z if $w > w_r$, applying to m the bumper force vector $\mathbf{f}_r = -f_r \hat{\mathbf{k}}$, where $f_r = 0$ if $w \leq w_r$ and $f_r = k_r(w - w_r) + c_r \dot{w}$ if $w > w_r$, with $\dot{w} = \nabla w^T \dot{\mathbf{q}}$. Although the elastic term due to k_r rigorously prevents f_r from being wholly non-conservative, still the bumping mechanism will be here termed dissipative for brevity.

2.2.5 The combination of the four dissipative mechanisms

The total dissipative force applied to m by the four mechanisms is given by $\mathbf{f}_d = \mathbf{f}_c + \mathbf{f}_p + \mathbf{f}_\mu + \mathbf{f}_r$. By applying Newton's 2nd Law to the mass m subjected to (i) its static weight $\boldsymbol{w} = -mg\hat{\mathbf{k}}$, (ii) the normal reaction force $\mathbf{N}$ at the contact point, and (iii) the total dissipative force $\mathbf{f}_d$, the dynamic equilibrium equation results as $\boldsymbol{w} + \mathbf{N} + \mathbf{f}_d = m(\boldsymbol{a} + \ddot{\mathbf{r}})$, where $\boldsymbol{a} + \ddot{\mathbf{r}}$ is the absolute acceleration of m. Denoting respectively by $\boldsymbol{\lambda_d} = m(\boldsymbol{a} + \ddot{\mathbf{r}})$ and by $\boldsymbol{\lambda_s} = -\boldsymbol{w}$ the dynamic and the static interaction forces exchanged between the BTMD and its support, and by $\mathbf{R} = \mathbf{N} + \mathbf{f}_\mu$ the total reaction force vector at the contact point, the same equilibrium equation provides $\mathbf{N} = \boldsymbol{\lambda_s} + \boldsymbol{\lambda_d} - \mathbf{f}_d$, which completely defines f_μ in Eq. (1).

2.3 The fully nonlinear 3D model of the absorber

The equation of motion of the absorber is here derived by applying the following Euler-Lagrange equation to the mass m [12,13]:

$$\frac{d}{dt}\left(\frac{\partial T}{\partial \dot{\mathbf{q}}}\right) - \frac{\partial T}{\partial \mathbf{q}} + \frac{\partial V_g}{\partial \mathbf{q}} + \boldsymbol{Q}_i + \boldsymbol{Q}_e = \mathbf{0} \tag{5}$$

where $T = \frac{m}{2}\dot{\mathbf{r}}^T\dot{\mathbf{r}}$ is the kinetic energy; $V_g = mgw$ is the gravitational potential energy; $\mathbf{Q}_i = -\mathbf{J}^T\mathbf{f}_d$ is the generalized internal force due to the total dissipative force $\mathbf{f}_d$ (representing the projection of $\mathbf{f}_d$ on the local tangent vectors $\frac{\partial \mathbf{r}}{\partial u}$ and $\frac{\partial \mathbf{r}}{\partial v}$); and $\mathbf{Q}_e = m\mathbf{J}^T\boldsymbol{a}$ is the generalized external force due to the support acceleration. By deriving the first three terms of Eq. (5) as specified in [12,13] and by denoting as $\mathbf{M}^q = m\mathbf{J}^T\mathbf{J}$ the generalized mass matrix of the absorber, the following nonlinear matrix differential equation is obtained, representing the fully nonlinear 3D BTMD model [13]:

$$\mathbf{M}^q\ddot{\mathbf{q}} + \mathbf{Q}_i + mg\nabla w = -m\mathbf{J}^T\boldsymbol{a} - \left(\dot{\mathbf{M}}^q\dot{\mathbf{q}} - \frac{\partial T}{\partial \mathbf{q}}\right) \tag{6}$$

where the three terms on the left-hand side respectively represent the generalized inertia force vector, the generalized dissipative force vector and the generalized gravitational restoring force vector, while the two

terms on the right-hand side respectively represent the generalized external force vector and a second-order term that couples $\mathbf{q}$ and $\dot{\mathbf{q}}$.
The dissipative term on the left-hand side is on its turn expressed by:

$$\mathbf{Q}_i = -\mathbf{J}^T\mathbf{f}_d = f_c\mathbf{J}^T\hat{\mathbf{c}} + f_p\mathbf{J}^T\hat{\mathbf{p}} + f_\mu\mathbf{J}^T\hat{\mathbf{t}} + f_r\mathbf{J}^T\hat{\mathbf{k}} \tag{7}$$

where the four terms on the right-hand side can be developed as follows:

$$f_c\mathbf{J}^T\hat{\mathbf{c}} = c\dot{s}_c\mathbf{J}^T\hat{\mathbf{c}} = c\left(\frac{\partial s_c}{\partial \mathbf{q}}\right)^T\dot{\mathbf{q}}\frac{\partial s_c}{\partial \mathbf{q}} = c[\boldsymbol{J}^T\hat{\boldsymbol{c}}\hat{\boldsymbol{c}}^T\boldsymbol{J}]\dot{\mathbf{q}} \tag{8}$$

$$f_p\mathbf{J}^T\hat{\mathbf{p}} = \text{sign}(\dot{s}_p)\,p\mathbf{J}^T\hat{\mathbf{p}} = \text{sign}\left(\left(\frac{\partial s_p}{\partial \mathbf{q}}\right)^T\dot{\mathbf{q}}\right)p\frac{\partial s_p}{\partial \mathbf{q}} = \text{sign}(\hat{\mathbf{p}}^T\mathbf{J}\dot{\mathbf{q}})p\mathbf{J}^T\hat{\mathbf{p}} \tag{9}$$

$$f_\mu\mathbf{J}^T\hat{\mathbf{t}} = \mu(\mathbf{q})N\,\mathbf{J}^T\mathbf{J}\dot{\mathbf{q}}/\sqrt{\dot{\mathbf{q}}^T\mathbf{J}^T\mathbf{J}\dot{\mathbf{q}}} \tag{10}$$

$$f_r\mathbf{J}^T\hat{\mathbf{k}} = f_r\nabla w \tag{11}$$

and represent, respectively, the generalized viscous, axial-friction, tangential-friction and bumper force vectors. Eqs. (8), (10) and (11) are already present in [13]. Eq. (9) is implicitly present in [12].

2.4 The fully nonlinear 3D model of the absorber on a linear MDOF structure

The dynamic equation of motion of a linear multi-degree-of-freedom (MDOF) structure equipped with the BTMD and subjected to external forces and ground accelerations is expressed by:

$$\mathbf{M}_s\ddot{\mathbf{q}}_s + \mathbf{C}_s\dot{\mathbf{q}}_s + \mathbf{K}_s\mathbf{q}_s + \mathbf{L}^T\boldsymbol{\lambda}_{\boldsymbol{d}} = \mathbf{f}_s - \mathbf{M}_s\mathbf{R}_s\ddot{\mathbf{r}}_g \tag{12}$$

where $\mathbf{q}_s$ is the structural DOFs vector; $\mathbf{M}_s$, $\mathbf{C}_s$ and $\mathbf{K}_s$ are the structural mass, damping and stiffness matrices; $\mathbf{f}_s$ is the external force vector; $\ddot{\mathbf{r}}_g = \begin{bmatrix}\ddot{u}_g & \ddot{v}_g & \ddot{w}_g\end{bmatrix}^T$ is the ground acceleration vector; $\boldsymbol{\lambda}_{\boldsymbol{d}}$ is the dynamic interaction force vector between the BTMD and its structural support; $\mathbf{L}$ is the kinematic transformation matrix; and $\mathbf{R}_s$ is the input topological matrix.
By expressing the absolute acceleration at the structural support as $\boldsymbol{a} = \mathbf{L}\left(\ddot{\mathbf{q}}_s + \mathbf{R}_s\ddot{\mathbf{r}}_g\right)$ and the relative acceleration of the BTMD as $\ddot{\mathbf{r}} = \mathbf{J}\ddot{\mathbf{q}} + \dot{\mathbf{J}}\dot{\mathbf{q}}$, the dynamic interaction force $\boldsymbol{\lambda}_{\boldsymbol{d}}$ in Eq. (12) can be given as [12,13]:

$$\boldsymbol{\lambda}_{\boldsymbol{d}} = m(\boldsymbol{a} + \ddot{\mathbf{r}}) = m\left(\mathbf{L}\ddot{\mathbf{q}}_s + \mathbf{L}\mathbf{R}_s\ddot{\mathbf{r}}_g + \mathbf{J}\ddot{\mathbf{q}} + \dot{\mathbf{J}}\dot{\mathbf{q}}\right) \tag{13}$$

By combining Eqs. (6), (12) and (13), the fully nonlinear 3D coupled equation of motion of the structure-BTMD combined system under external force and ground acceleration input is finally obtained as:

$$\begin{bmatrix}\mathbf{M}_s + m\mathbf{L}^T\mathbf{L} & m\mathbf{L}^T\mathbf{J} \\ m\mathbf{J}^T\mathbf{L} & \mathbf{M}^q\end{bmatrix}\begin{bmatrix}\ddot{\mathbf{q}}_s \\ \ddot{\mathbf{q}}\end{bmatrix} + \begin{bmatrix}\mathbf{C}_s & \mathbf{0} \\ \mathbf{0} & \mathbf{0}\end{bmatrix}\begin{bmatrix}\dot{\mathbf{q}}_s \\ \dot{\mathbf{q}}\end{bmatrix} + \begin{bmatrix}\mathbf{0} \\ \mathbf{Q}_i\end{bmatrix} + \begin{bmatrix}\mathbf{K}_s & \mathbf{0} \\ \mathbf{0} & \mathbf{0}\end{bmatrix}\begin{bmatrix}\mathbf{q}_s \\ \mathbf{q}\end{bmatrix} =$$
$$= \begin{bmatrix}\mathbf{f}_s \\ \mathbf{0}\end{bmatrix} - \begin{bmatrix}\mathbf{M}_s + m\mathbf{L}^T\mathbf{L} \\ m\mathbf{J}^T\mathbf{L}\end{bmatrix}\mathbf{R}_s\ddot{\mathbf{r}}_g - \begin{bmatrix}m\mathbf{L}^T\dot{\mathbf{J}}\dot{\mathbf{q}} \\ \dot{\mathbf{M}}^q\dot{\mathbf{q}} - \frac{\partial T}{\partial \mathbf{q}}\end{bmatrix} \tag{14}$$

2.5 The first-order 3D model

By developing in Taylor series each expression of Eqs. (7) to (11) and by truncating higher-order terms, the first-order approximation of the fully nonlinear 3D model of the absorber is obtained as in [12,13]. In particular, the various terms are approximated as follows:

- the generalized inertia force vector in Eq. (6) becomes $\mathbf{M}^q\ddot{\mathbf{q}} \approx m\ddot{\mathbf{q}}$;
- the surface gradient vector in Eq. (6) becomes $\nabla w \approx \mathbf{H}_w\mathbf{q}$, where [12,13]:

$$\mathbf{H}_w = \begin{bmatrix}1/L_x & 0 \\ 0 & 1/L_y\end{bmatrix} = \begin{bmatrix}h_{wx} & 0 \\ 0 & h_{wy}\end{bmatrix} \tag{15}$$

  is the Hessian matrix of $w(\mathbf{q})$ in $\mathbf{q} = \mathbf{0}$, and L_x and L_y are the pendulum lengths along x and y, with $L_x \le L_y$ all through this paper, by convention;
- the generalized restoring force vector in Eq. (6) becomes $mg\nabla w \approx mg\mathbf{H}_w\mathbf{q} = \mathbf{K}_w\mathbf{q}$, where [12,13]:

$$\mathbf{K}_w = \begin{bmatrix}mg/L_x & 0 \\ 0 & mg/L_y\end{bmatrix} = \begin{bmatrix}k_{wx} & 0 \\ 0 & k_{wy}\end{bmatrix} \tag{16}$$

  is the equivalent pendulum stiffness matrix, and k_{wx} and k_{wy} are the equivalent pendulum stiffness coefficients along x and y;

- the generalized viscous force vector in Eq. (8), assuming that the undeformed viscous damper lies in the xy plane, becomes [13]:

$$f_c \mathbf{J}^T \hat{\mathbf{c}} \approx c\left[\hat{\mathbf{c}}_{0h}\hat{\mathbf{c}}_{0h}^T\right] = c\begin{bmatrix} \hat{c}_{0x}^2 & \hat{c}_{0x}\hat{c}_{0y} \\ \hat{c}_{0x}\hat{c}_{0y} & \hat{c}_{0y}^2 \end{bmatrix}\dot{\mathbf{q}} = \mathbf{C}\dot{\mathbf{q}} \tag{17}$$

  where $\hat{\mathbf{c}}_{0h} = \hat{\mathbf{c}}_0(1{:}\,2) = \left[\hat{c}_{0x}, \hat{c}_{0y}\right]^T$ and $\mathbf{C}$ is the BTMD viscous damping matrix;
- the generalized friction force vector in Eq. (9), assuming that the undeformed friction damper is vertically oriented, becomes [12]:

$$f_p \mathbf{J}^T \hat{\mathbf{p}} \approx f_p \mathbf{H}_p \mathbf{q} = \text{sign}\left(\dot{s}_p\right) p \mathbf{H}_p \mathbf{q} = \text{sign}\left(\dot{s}_p\right) \mathbf{K}_p \mathbf{q} \tag{18}$$

  where:

$$\mathbf{H}_p = \begin{bmatrix} 1/L_x + 1/l_{p0} & 0 \\ 0 & 1/L_y + 1/l_{p0} \end{bmatrix} = \begin{bmatrix} h_{px} & 0 \\ 0 & h_{py} \end{bmatrix} \tag{19}$$

  is the Hessian matrix of $s_p(\mathbf{q})$ in $\mathbf{q} = \mathbf{0}$,

$$\mathbf{K}_p = p\mathbf{H}_p = p\begin{bmatrix} h_{px} & 0 \\ 0 & h_{py} \end{bmatrix} = \begin{bmatrix} k_{px} & 0 \\ 0 & k_{py} \end{bmatrix} \tag{20}$$

  is the equivalent axial-friction stiffness matrix, and

$$\dot{s}_p = \mathbf{q}^T {\mathbf{H}_p}^T \dot{\mathbf{q}} = h_{px} u\dot{u} + h_{py} v\dot{v} \tag{21}$$

  is the first-order approximation of the friction damper axial elongation rate.
- the friction coefficient in Eq. (10), assuming the friction pattern expressed by Eq. (2), becomes:

$$\mu(\mathbf{q}) \approx \|\boldsymbol{\mu}_\mathbf{0}\mathbf{H}_w\mathbf{q}\| \tag{22}$$

- the normal component of the reaction force vector in Eq. (10) becomes [13]:

$$N \approx m(g + a_z) = mgN_0 \tag{23}$$

  where its weight-normalized expression $N_0 = N/mg = (1 + a_z/g)$ has been introduced;
- the generalized friction force vector in Eq. (10), considering Eqs. (22) and (23) and observing that $\mathbf{J}^T\mathbf{J}\dot{\mathbf{q}} \approx \dot{\mathbf{q}}$ and $\sqrt{\dot{\mathbf{q}}^T\mathbf{J}^T\mathbf{J}\dot{\mathbf{q}}} \approx \sqrt{\dot{\mathbf{q}}^T\dot{\mathbf{q}}} = \|\dot{\mathbf{q}}\|$, becomes [13]:

$$f_\mu \mathbf{J}^T\hat{\mathbf{t}} \approx\ mgN_0\|\boldsymbol{\mu}_\mathbf{0}\mathbf{H}_w\mathbf{q}\|\,\dot{\mathbf{q}}/\|\dot{\mathbf{q}}\| = N_0\|\boldsymbol{\mu}_\mathbf{0}\mathbf{K}_w\mathbf{q}\|\,\dot{\mathbf{q}}/\|\dot{\mathbf{q}}\| \tag{24}$$

- the generalized bumper force in Eq. (11), observing that the bumper is not activated in the small-displacement domain, becomes $f_r\mathbf{J}^T\hat{\mathbf{k}} = \mathbf{0}$;
- the generalized external force vector in Eq. (6) becomes $-m\mathbf{J}^T\boldsymbol{a} = -m\boldsymbol{a}_h - m\nabla w \approx -m\boldsymbol{a}_h - a_z/g\,\mathbf{K}_w\mathbf{q}$, where $\boldsymbol{a}_h = \boldsymbol{a}(1{:}\,2) = \left[a_x, a_y\right]^T$ and $a_z = \boldsymbol{a}(3)$ are the horizontal and vertical components of the vector of support accelerations, respectively;
- the second-order term in Eq. (6) becomes $\dot{\mathbf{M}}^q\dot{\mathbf{q}} - \frac{\partial T}{\partial \mathbf{q}} \approx \mathbf{0}$.

With the approximations listed above, the first-order 3D model of the BTMD finally becomes:

$$m\ddot{\mathbf{q}} + \mathbf{C}\dot{\mathbf{q}} + N_0\mathbf{K}_w\mathbf{q} + \text{sign}\left(\dot{s}_p\right)\mathbf{K}_p\mathbf{q} + N_0\|\boldsymbol{\mu}_\mathbf{0}\mathbf{K}_w\mathbf{q}\|\,\dot{\mathbf{q}}/\|\dot{\mathbf{q}}\| = -m\boldsymbol{a}_h \tag{25}$$

and the first-order 3D model of the coupled structure-BTMD system becomes:

$$\begin{bmatrix} \mathbf{M}_s + m\mathbf{L}_h^T\mathbf{L}_h & m\mathbf{L}_h^T \\ m\mathbf{L}_h & m\mathbf{I} \end{bmatrix}\begin{bmatrix} \ddot{\mathbf{q}}_s \\ \ddot{\mathbf{q}} \end{bmatrix} + \begin{bmatrix} \mathbf{C}_s & \mathbf{0} \\ \mathbf{0} & \mathbf{C} + N_0\,\|\boldsymbol{\mu}_\mathbf{0}\mathbf{K}_w\mathbf{q}\|/\|\dot{\mathbf{q}}\| \end{bmatrix}\begin{bmatrix} \dot{\mathbf{q}}_s \\ \dot{\mathbf{q}} \end{bmatrix} + \\ + \begin{bmatrix} \mathbf{K}_s & \mathbf{0} \\ \mathbf{0} & N_0\mathbf{K}_w + \text{sign}(\dot{s}_p)\mathbf{K}_p \end{bmatrix}\begin{bmatrix} \mathbf{q}_s \\ \mathbf{q} \end{bmatrix} = \begin{bmatrix} \mathbf{f}_s \\ \mathbf{0} \end{bmatrix} - \begin{bmatrix} \mathbf{M}_s + m\mathbf{L}_h^T\mathbf{L}_h \\ m\mathbf{L}_h \end{bmatrix}\mathbf{R}_s\ddot{\mathbf{r}}_g \tag{26}$$

where $\mathbf{L}_h = \mathbf{L}(1{:}\,2)$ are the first two columns of $\mathbf{L}$, and $\dot{s}_p$ is given by Eq. (21).

The following fundamental properties of the BTMD, valid in the small-displacement domain, are expressed by Eq. (25):

(i) the inertia force vector $m\ddot{\mathbf{q}}$ and the restoring force vector $N_0\mathbf{K}_w\mathbf{q}$ are linear and uncoupled along x and y; if multiple viscous dampers are modelled, the viscous force vector $\mathbf{C}\dot{\mathbf{q}}$ in Eq. (25) results from the summation of their respective contributions, each computed according to Eq. (17); if, as here assumed, all viscous dampers lie in the horizontal plane, $\mathbf{C}\dot{\mathbf{q}}$ is linear too and independent from the length of the dampers, though not uncoupled unless every damper is parallel to either x or y, which would make $\mathbf{C}$ diagonal;

(ii) through the N_0 term, the vertical support acceleration a_z affects the horizontal response of the BTMD even in the first-order model, entering both the restoring force and the tangential-friction force vectors;
(iii) the generalized axial-friction force vector $\text{sign}(\dot{s}_p)\mathbf{K}_p\mathbf{q}$ has modulus and direction defined by the product $\mathbf{K}_p\mathbf{q}$, linear in $\mathbf{q}$ and radially oriented, but has the sign of $\dot{s}_p$, which, according to Eq. (21), ultimately makes it a nonlinear coupled function of $\mathbf{q}$ and $\dot{\mathbf{q}}$;
(iv) the generalized tangential-friction force vector $N_0\|\boldsymbol{\mu}_\mathbf{0}\mathbf{K}_w\mathbf{q}\|\,\dot{\mathbf{q}}/\|\dot{\mathbf{q}}\|$ has modulus $N_0\|\boldsymbol{\mu}_\mathbf{0}\mathbf{K}_w\mathbf{q}\|$ and has direction and sign of the tangent versor $\dot{\mathbf{q}}/\|\dot{\mathbf{q}}\|$; because modulus, direction and sign are nonlinear and coupled, the generalized tangential-friction force vector too is a nonlinear coupled function of $\mathbf{q}$ and $\dot{\mathbf{q}}$;
(v) both the generalized axial-friction and tangential-friction force vectors are homogeneous functions of $\mathbf{q}$ and $\dot{\mathbf{q}}$ (i.e. functions proportionally affected by any arbitrary scalar γ factor of $\mathbf{q}$ and $\dot{\mathbf{q}}$); because all terms on the left-hand side of Eq. (25) are also homogeneous, the equation itself is homogeneous and its solution is proportional to the horizontal acceleration $\boldsymbol{a}_h$ appearing at the right-hand side (not to the vertical acceleration a_z, though), which makes each friction BTMD a first-order nonlinear but homogeneous system.

2.6 The simplified 2D model

In order to establish an optimal BTMD design method, it is convenient to further simplify the 3D first-order models by assuming that: (i) the problem is planar in one vertical coordinate plane, so the 3D model degenerates into a 2D model in that plane; (ii) in that plane, the structural target frequency is far from the other structural frequencies, so the MDOF structure can be modelled as a 1DOF mode-generalized system [16]; (iii) the vertical acceleration input a_z is negligible (i.e. $N_0 = 1$). Under these conditions, assuming with no loss of generality that the said vertical plane is xz, Eqs. (25) and (26) respectively become:

$$m\ddot{u} + c_x\dot{u} + k_{wx}[1 + \text{sign}(u\dot{u})\chi_x + \text{sign}(u\dot{u})\mu_{0x}]u = -ma_x \tag{27}$$

and:

$$\begin{bmatrix} m_{sx}+m & m \\ m & m \end{bmatrix}\begin{bmatrix} \ddot{u}_s \\ \ddot{u} \end{bmatrix} + \begin{bmatrix} c_{sx} & 0 \\ 0 & c_x \end{bmatrix}\begin{bmatrix} \dot{u}_s \\ \dot{u} \end{bmatrix} + \begin{bmatrix} k_{sx} & 0 \\ 0 & k_{wx}[1 + \text{sign}(u\dot{u})\chi_x + \text{sign}(u\dot{u})\mu_{0x}] \end{bmatrix}\begin{bmatrix} u_s \\ u \end{bmatrix} = \\ = \begin{bmatrix} f_{sx} \\ 0 \end{bmatrix} - \begin{bmatrix} m_{sx}+m \\ m \end{bmatrix}\ddot{u}_g \tag{28}$$

where u_s is the relative displacement of the main structure along x; m_{sx}, c_{sx} and k_{sx} are the generalized mass, damping coefficient and stiffness of the main structure along x; f_{sx} is the external force acting on the main structure along x; c_x is the viscous damping coefficient of the BTMD along x; and

$$\chi_x = \frac{k_{px}}{k_{wx}} = \frac{p}{mg}\left(1 + \frac{L_x}{l_{p0}}\right) \tag{29}$$

is the axial-friction damping ratio along x.
Dividing Eq. (27) and the second line of Eq. (28) by m, and the first line of Eq. (28) by m_{sx}, Eqs. (27) and (28) can be respectively recast in modal terms as follows:

$$\ddot{u} + 2\zeta_x\omega_x\dot{u} + \omega_x^2[1 + \text{sign}(u\dot{u})\chi_x + \text{sign}(u\dot{u})\mu_{0x}]u = -a_x \tag{30}$$

$$\begin{bmatrix} 1+m_{Rx} & m_{Rx} \\ 1 & 1 \end{bmatrix}\begin{bmatrix} \ddot{u}_s \\ \ddot{u} \end{bmatrix} + 2\omega_{sx}\begin{bmatrix} \zeta_{sx} & 0 \\ 0 & \zeta_x\omega_{Rx} \end{bmatrix}\begin{bmatrix} \dot{u}_s \\ \dot{u} \end{bmatrix} + \\ +\omega_{sx}^2\begin{bmatrix} 1 & 0 \\ 0 & \omega_{Rx}^2[1 + \text{sign}(u\dot{u})\chi_x + \text{sign}(u\dot{u})\mu_{0x}] \end{bmatrix}\begin{bmatrix} u_s \\ u \end{bmatrix} = \begin{bmatrix} \bar{f}_{sx} \\ 0 \end{bmatrix} - \begin{bmatrix} 1+m_{Rx} \\ 1 \end{bmatrix}\ddot{u}_g \tag{31}$$

where $m_{Rx} = m/m_{sx}$ is the BTMD mass ratio along x; $\omega_{sx} = \sqrt{k_{sx}/m_s}$ and $\omega_x = \sqrt{g/L_x} = \sqrt{k_{wx}/m}$ are the circular frequencies of the main structure and of the BTMD along x; $\omega_{Rx} = \omega_x/\omega_{sx}$ is the BTMD frequency ratio along x; $\zeta_{sx} = c_{sx}/(2\omega_{sx}m_{sx})$ and $\zeta_x = c_x/(2\omega_x m)$ are the viscous damping ratios of the main structure and the BTMD along x; and $\bar{f}_{sx} = f_{sx}/m_{sx}$ is the mass-normalized external force acting on the main structure along x.
Significantly, Eqs. (27), (28), (30) and (31) show that the first-order 2D analytical models of the two friction mechanisms are identical, but for the fact that their respective multiplicative factor is χ_x for the axial friction and μ_{0x} for the tangential friction. This was not the case for the first-order 3D models of

Eqs. (25) and (26). This result proves that the same optimization criterion and the same response are expected for the two friction options in 2D problems, whereas a different performance is expected in 3D problems.
According to Eq. (31), once the structure and the external input are assigned, the first-order response of the system entirely depends on the five dimensionless parameters m_{Rx}, ω_{Rx}, ζ_x , χ_x and μ_{0x}, which completely define the BTMD and whose optimization is left to the following Section 3.

3. The design method

In this section, assuming the three damping types as mutually exclusive, the models derived in Section 2 are used to establish an optimal design method for a BTMD of either viscous type (V-BTMD) or homogeneous axial-friction type (HA-BTMD) or homogeneous tangential-friction type (HT-BTMD), with the aim of minimizing the displacement response of the structure to external force excitations. For any BTMD type, the design procedure comprises three stages, namely: (i) a 2D first-order optimization, (ii) a 3D first-order reconciliation and (iii) a 3D design completion, which develop as follows.

3.1 The 2D first-order optimization

The first stage consists in the optimization of the parameters of the BTMD under the main assumption that its motion be uncoupled along x and y and confined to the small-displacement domain. If, moreover, the main structure can be schematized, in each horizontal direction, as a SDOF linear system under an external force input, then the optimization can be separately conducted along x and y based on the simplified 2D model presented in Section 2.6, formalized by Eq. (31) along x and by an analogue expression along y. Because the HA-BTMD and the HT-BTMD are described by the same 2D model, the procedure is unique for the two friction options.
Referring to the x direction for simplicity, optimization is here posed according to two possible classical design criteria. The first one is the H_∞ design criterion, aimed at the minimization of the worst-case steady-state structural response to a unit-amplitude harmonic input [5]. The second one is the H_2 design criterion, aimed at the minimization of the root-mean-square (rms) structural response to a stationary Gaussian zero-mean white-noise input [17]. The two criteria have been widely used in the past to design linear TMDs [16], and the H_∞ criterion has been recently used by the author in [13] to design homogeneous friction TMDs on a structure undergoing ground accelerations. However, none of the two criteria has ever been applied to homogeneous friction TMDs on structures subjected to force excitations, and the H_2 criterion has never been rigorously applied to homogeneous friction TMDs at all. In this section, the H_∞ and the H_2 optimal design problems are set and solved for the V-BTMD and the two H-BTMD types, for a force input acting on the main structure. The H_∞-optimal and the H_2-optimal BTMDs are subsequently evaluated through first an H_∞ performance analysis and then an H_2 performance analysis, to illustrate the trade-off between the two design options.
Assuming the structure known and the BTMD mass ratio established according to cost-benefit expectations, the only two free design parameters, i.e. the frequency ratio and the damping ratio for the V-BTMD and the frequency ratio and the friction ratio for both H-BTMD types, are determined by minimizing either the H_∞ norm or the H_2 norm of a selected input-output transfer function of the structure-BTMD system. Denoting with ω the circular frequency of the external force input, the adopted transfer function is here the force-to-displacement transfer function $T_{u_s\bar{f}_{sx}}(\omega)$, computed from $\bar{f}_{sx}$ to u_s. Introducing the response ratio $R_x = \|T_{u_s\bar{f}_{sx}}\|_n^{con} / \|T_{u_s\bar{f}_{sx}}\|_n^{unc}$ as the ratio of the controlled to the uncontrolled H_n norm of $T_{u_s\bar{f}_{sx}}(\omega)$ (n standing either for ∞ or for 2), both the H_∞ and the H_2 optimization problems can be formalized as follows:
(i) for the V-BTMD:

$$R_{xopt} = \min_{\omega_{Rx},\zeta_x} R_x \tag{32}$$

(ii) for the HA-BTMD:

$$R_{xopt} = \min_{\omega_{Rx},\chi_x} R_x \tag{33}$$

(iii) for the HT-BTMD:

$$R_{xopt} = \min_{\omega_{Rx},\mu_{0x}} R_x \tag{34}$$

which respectively provide the V-BTMD optimal parameters ω_{Rxopt} and ζ_{xopt}, the HA-BTMD optimal parameters ω_{Rxopt} and χ_{xopt}, and the HT-BTMD optimal parameters ω_{Rxopt} and μ_{0xopt}. Because of the said equivalence between the two friction models, Eqs. (33) and (34) are in fact the same problem and produce the same optimal solution, valid for both H-BTMD types. Moreover, because R_x only depends on the structural damping ratio ζ_{sx} and on the dimensionless BTMD parameters, the solutions to Eqs. (32) to (34) turn out to exclusively depend on ζ_{sx} and m_{Rx}.

Of the three optimization problems above, Eq. (32) is the classical formulation for linear TMDs, already solved analytically for undamped structures and numerically for damped structures, both in H_∞ and in H_2 terms [16,5,18,19]. Eqs. (33) and (34) are instead new. Their solution is here obtained through a numerical optimization, based on a branch and bound algorithm followed by a nonlinear least-square solver. The objective function R_x, which can be computed in an exact way for the linear system in Eq. (32), can only be computed in an approximate way for the nonlinear system in Eqs. (33) or (34), no matter if the H_∞ or the H_2 strategy is adopted. In the H_∞ case, the transfer function $T_{u_s\bar{f}_{sx}}$, which for the linear system in Eq. (32) admits a closed-form expression, must be computed by points for the nonlinear system in Eqs. (33) or (34), i.e. through simulating the system separately under each harmonic input frequency, until the response amplitude becomes acceptably steady. The maximum of $T_{u_s\bar{f}_{sx}}$ over all the explored frequencies provides the desired H_∞ norm. In the H_2 case, the stationary rms response, which for the linear system can be obtained from the output covariance matrices by solving the classical Lyapunov equation [20], must be computed through Monte Carlo simulations for the nonlinear system, i.e. by averaging the rms response of the system to several realizations of the stochastic input process. To achieve a satisfactory stabilization, 200 realizations are here considered, each one having duration $t_{tot} = 3600T_{sx}$ and sampling time $t_s = 0.01T_{sx}$, where $T_{sx} = 2\pi/\omega_{sx}$ is the period of the main structure.

For $\zeta_{sx} = 2\%$ and $m_{Rx} = 3\%$, the solution of the H_∞ optimization problem is reported in Figure 2a, where the transfer functions drawn for, respectively, the optimal V-BTMD and the optimal H-BTMD appear nearly identical, with the H-BTMD transfer function slightly lower and shifted rightwards. Figures 2b to 2d report, for the same two optimal absorbers, the time response of the system under the first 15 cycles of a sinusoidal input, $\bar{f}_{sx} = \bar{f}_{sx0}\sin(\omega_{sx}t)$, applied at the frequency of the uncontrolled structure. For generality, all displacements are normalized to the static displacement amplitude $u_{s0} = m_{sx}\bar{f}_{sx0}/k_{sx} = \bar{f}_{sx0}/\omega_{sx}^2$ and all forces to the equivalent force amplitude $m_{sx}\bar{f}_{sx0}$. In particular, Figures 2b and 2c report the time-histories of the normalized displacements of, respectively, the structure and the BTMD, while Figure 2d reports the normalized hysteresis loops of the BTMD, with f_{dx} denoting the x component of the dissipative force $\mathbf{f}_d$. Like Figure 2a, Figures 2b and 2c show that the V-BTMD and the H-BTMD produce similar overall results. Figure 2d shows the different constitutive laws of the two mechanisms, which result in elliptic loops for the V-BTMD and in triangular loops for the H-BTMD, but which provide a nearly identical cyclic energy dissipation, independently from the excitation amplitude. Denoting by u_{max} the steady-state displacement amplitude of the H-BTMD, by E_d its cyclic energy dissipation, equalling $2k_{wx}\chi_x u_{max}^2$ for the HA-BTMD and $2k_{wx}\mu_{0x}u_{max}^2$ for the HT-BTMD, and by $E_w = \frac{1}{2}\,k_{wx}u_{max}^2$ its maximum stored potential energy, the equivalent viscous damping ratio of the H-BTMD can be classically expressed as $\zeta_{x,eq} = \frac{1}{4\pi}\frac{E_d}{E_w}$ and turns out to equal χ_x/π for the HA-BTMD and μ_{0x}/π for the HT-BTMD.

By repeating the H_∞ optimization for m_{Rx} ranging from 1‰ to 20%, Table 1 and Figure 3 are obtained, which provide the H_∞-optimal dimensionless parameters and the corresponding H_∞ response ratios for the V-BTMD and for both H-BTMD types. For convenience, in both Table 1 and Figure 3b the optimal friction ratios χ_{xopt} and μ_{0xopt} are expressed in terms of equivalent viscous damping, i.e. divided by π.

Referring to the V-BTMD (red dotted lines), Figure 3 shows well-known trends, with both ω_{Rxopt} and R_{xopt} decreasing from 1, and ζ_{xopt} increasing from 0. Referring to the H-BTMD (blue continuous lines), Figure 3 shows that: (i) ω_{Rxopt} decreases from 1 much less rapidly than in the viscous case: the larger the mass ratio, the stiffer the optimal H-BTMD w.r.t. the optimal V-BTMD (i.e. the more concave the H-

BTMD profile w.r.t. the V-BTMD profile); (ii) χ_{xopt}/π and μ_{0xopt}/π are lower than ζ_{xopt} but converge to it as m_{Rx} tends to zero; (iii) R_{xopt} is nearly identical but systematically smaller than its viscous counterpart; therefore, if correctly optimized, homogeneous friction proves even more effective than viscous damping for TMD applications. Beside the V-BTMD (red line) and the H-BTMD (blue line), Figure 3c also presents a third type of BTMD (green line), denoted as the H-BTMD*, here defined, as in [12], as the suboptimal H-BTMD whose frequency ratio ω_{Rxopt} equals that of the optimal V-BTMD (red line in Figure 2b), and whose equivalent viscous damping ratio, χ_{xopt}/π or μ_{0xopt}/π, equals the damping ratio ζ_{xopt} of the optimal V-BTMD (red line in Figure 3b). Clearly from Figure 3, the H-BTMD* appears as effective as the optimal H-BTMD for very small values of m_{Rx}, i.e. when the optimal parameters for the H-BTMD and for the V-BTMD tend to coincide (Figures 3a and 3b), but less effective for larger values of m_{Rx}, when the optimal H-BTMD gets much stiffer and less damped than its viscous counterpart. For $m_{Rx} = 10\%$, e.g., R_{xopt} is 35% larger for the H-BTMD* than for the H-BTMD.

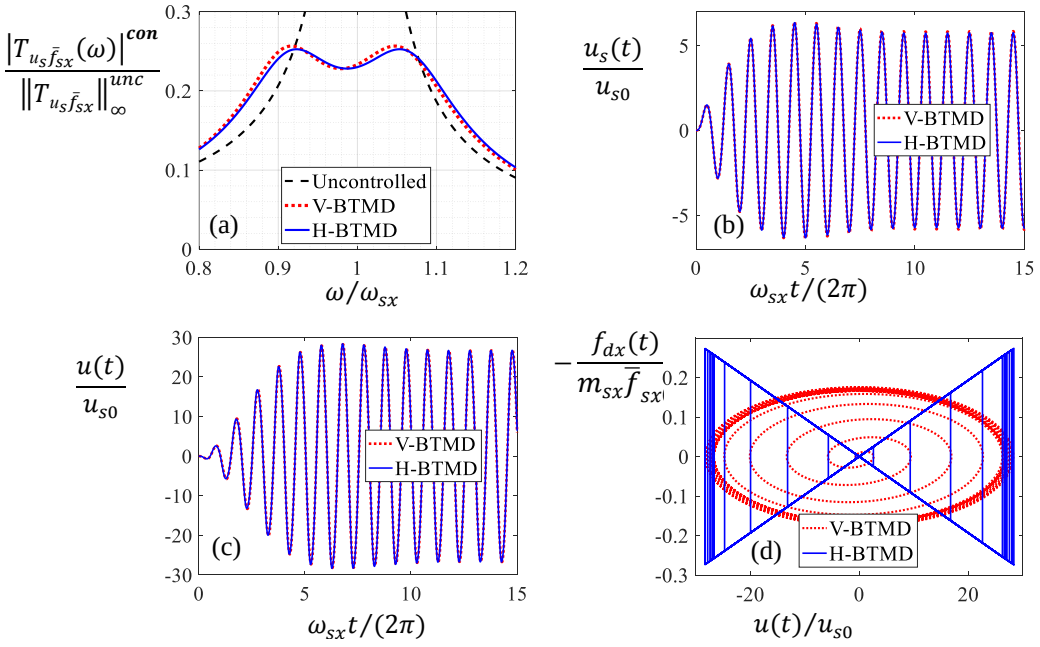

Figure 2. Frequency and time response of a structure-BTMD system under harmonic force input, for ζ_{sx} = 2% and m_{Rx} = 3%: (a) transfer function; (b) structural displacement; (c) BTMD stroke; (d) BTMD constitutive law.

Table 1. H_∞ optimal design of V-BTMDs and H-BTMDs under force excitation as a function of m_{Rx}, for ζ_{sx} = 2%.

m_{Rx}	V-BTMD			H-BTMD		
	ω_{Rxopt}	ζ_{xopt}	R_{xopt}	ω_{Rxopt}	χ_{0xopt}/π ; μ_{0xopt}/π	R_{xopt}
0.001	0.9977	0.0221	0.6807	0.9988	0.0221	0.6802
0.002	0.9963	0.0301	0.5916	0.9983	0.0300	0.5909
0.005	0.9926	0.0460	0.4681	0.9973	0.0458	0.4669
0.010	0.9869	0.0638	0.3785	0.9958	0.0632	0.3765
0.020	0.9761	0.0887	0.2981	0.9932	0.0871	0.2950
0.030	0.9658	0.1076	0.2566	0.9907	0.1045	0.2526
0.040	0.9558	0.1233	0.2298	0.9883	0.1185	0.2251
0.050	0.9461	0.1370	0.2106	0.9857	0.1302	0.2053
0.060	0.9366	0.1491	0.1960	0.9832	0.1403	0.1902
0.070	0.9274	0.1602	0.1843	0.9804	0.1485	0.1780

0.080	0.9184	0.1704	0.1747	0.9779	0.1564	0.1681
0.090	0.9095	0.1798	0.1666	0.9750	0.1629	0.1596
0.100	0.9009	0.1886	0.1596	0.9722	0.1690	0.1524
0.120	0.8841	0.2046	0.1483	0.9670	0.1808	0.1406
0.140	0.8680	0.2190	0.1393	0.9615	0.1901	0.1313
0.160	0.8525	0.2321	0.1320	0.9558	0.1982	0.1237
0.180	0.8376	0.2441	0.1259	0.9501	0.2052	0.1174
0.200	0.8232	0.2552	0.1207	0.9445	0.2113	0.1121

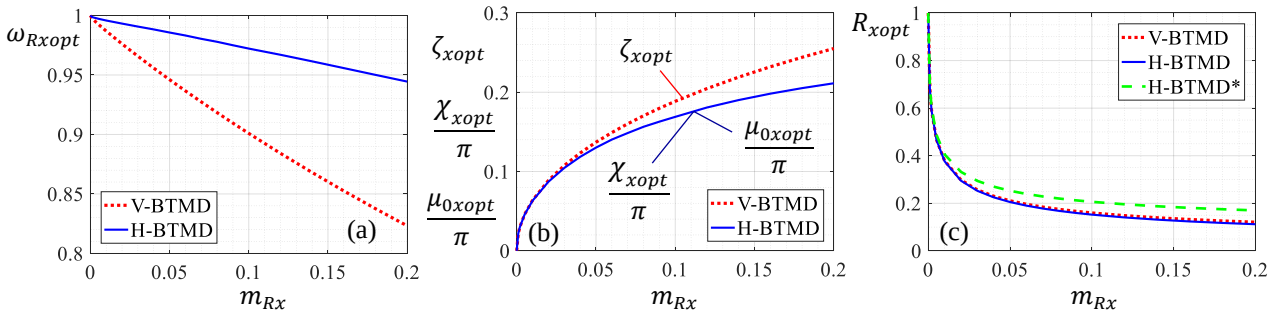

Figure 3. H_∞ optimal design of the V-BTMD and the H-BTMD under force excitation as a function of m_{Rx}, for ζ_{sx} = 2%: (a) optimal frequency ratios; (b) optimal damping ratios; (c) optimal response ratios (including the H-BTMD* option).

Similarly, Table 2 and Figure 4 report the results of the H_2 optimization problem. The overall trends recognized in Table 1 and Figure 3 for the H_∞ case are here confirmed, with the optimal parameters only slightly modified (Figures 4a and 4b) and the optimal response ratios obviously increased (Figure 4c), as it is always the case whenever a TMD is evaluated in H_∞ terms rather than in H_2 terms. Strongly reduced are, however, the differences between the response ratios corresponding to, respectively, the optimal H-BTMD and the suboptimal H-BTMD* (Figure 4c), with the latter being now defined based on the parameters of the H_2-optimal V-BTMD. For $m_{Rx} = 10\%$, e.g., R_{xopt} is only 2% larger for the H-BTMD* than for the H-BTMD. Clearly, the H-BTMD* approximates the optimal H-BTMD much better when the design is conducted in H_2 terms than in H_∞ terms. Because the H-BTMD and the H-BTMD* are still characterized by significantly different parameters, this good approximation reveals the greater insensitivity of the H_2 performance to deviations of the TMD parameters from optimality, w.r.t. the H_∞ performance.

Table 2. H_2 optimal design of V-BTMDs and H-BTMDs under force excitation as a function of m_{Rx}, for ζ_{sx} = 2%.

m_{Rx}	V-BTMD			H-BTMD		
	ω_{Rxopt}	ζ_{xopt}	R_{xopt}	ω_{Rxopt}	χ_{0xopt}/π ; μ_{0xopt}/π	R_{xopt}
0.001	0.9989	0.0158	0.8972	0.9990	0.0159	0.8974
0.002	0.9981	0.0223	0.8493	0.9988	0.0226	0.8494
0.005	0.9956	0.0353	0.7693	0.9981	0.0357	0.7691
0.010	0.9916	0.0498	0.6996	0.9972	0.0504	0.6994
0.020	0.9839	0.0702	0.6259	0.9956	0.0703	0.6257
0.030	0.9765	0.0856	0.5823	0.9938	0.0857	0.5822
0.040	0.9693	0.0985	0.5518	0.9922	0.0990	0.5517
0.050	0.9622	0.1098	0.5284	0.9905	0.1095	0.5284
0.060	0.9553	0.1198	0.5095	0.9888	0.1192	0.5095
0.070	0.9485	0.1290	0.4937	0.9871	0.1278	0.4939

0.080	0.9418	0.1374	0.4803	0.9853	0.1358	0.4805
0.090	0.9353	0.1452	0.4686	0.9835	0.1430	0.4690
0.100	0.9289	0.1525	0.4582	0.9815	0.1498	0.4588
0.120	0.9165	0.1660	0.4405	0.9777	0.1623	0.4415
0.140	0.9045	0.1781	0.4259	0.9734	0.1733	0.4273
0.160	0.8929	0.1891	0.4135	0.9690	0.1833	0.4152
0.180	0.8817	0.1993	0.4026	0.9644	0.1924	0.4048
0.200	0.8708	0.2087	0.3931	0.9598	0.2007	0.3957

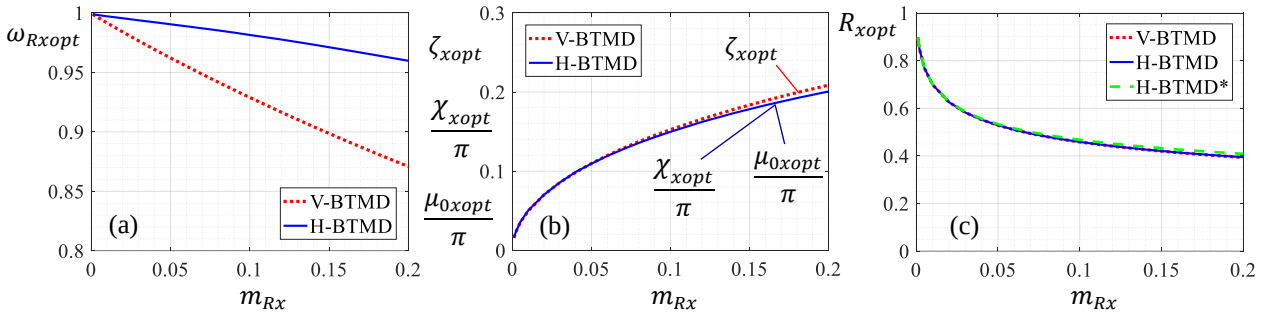

Figure 4. H_2 optimal design of the V-BTMD and the H-BTMD under force excitation as a function of m_{Rx}, for ζ_{sx} = 2%: (a) optimal frequency ratios; (b) optimal damping ratios; (c) optimal response ratios (including the H-BTMD* option).

To clarify this point, Figure 5 shows the H_∞ and the H_2 response ratios obtained for a V-BTMD (red lines, on the left) and for an H-BTMD (blue lines, on the right), each optimized according to either the H_∞ criterion or the H_2 criterion. For both BTMD types, it appears that the H_2 response is not much influenced by the adopted design criterion (the two higher curves in each figure are quite coincident, with the H_2-designed BTMD outperforming the H_∞-designed BTMD by less than 1.7%), whilst the H_∞ response significantly depends on the adopted design criterion (the two lower curves in each figure show large differences, with the H_∞-designed BTMD outperforming the H_2-designed BTMD by more than 18%). This suggests that the H_∞ design is generally more robust than the H_2 design for TMD applications and should be practically preferred whenever the excitation might possibly switch from a random input to a harmonic input concentrated in the frequency range of the main structure. Also, replacing the H_2 design with the H_∞ design affects the H_2 response ratios of the V-BTMD and the H-BTMD by substantially the same percentage, keeping their relative performance unchanged. For these reasons, in the remaining of this paper the H_∞ design will be considered as the standard approach and systematically adopted in all simulations.

What obtained above in the x direction equally holds in the y direction too, as long as the BTMD motion is supposed uncoupled. If, additionally, the two structural target modes along x and y have the same damping ratio $\zeta_{sx} = \zeta_{sy} = \zeta_s$ and the same generalized mass $m_{sx} = m_{sy} = m_s$, as it will be constantly assumed in the sequel for simplicity, then the BTMD will have the same mass ratio $m_{Rx} = m_{Ry} = m_R$ and therefore the same dimensionless optimal parameters along x and y: $\omega_{Rxopt} = \omega_{Ryopt} = \omega_{Ropt}$, $\zeta_{xopt} = \zeta_{yopt} = \zeta_{opt}$, $\chi_{xopt} = \chi_{yopt} = \chi_{opt}$, and $\mu_{0xopt} = \mu_{0yopt} = \mu_{0opt}$. The physical soundness of these parameters is discussed in Section 3.2 next.

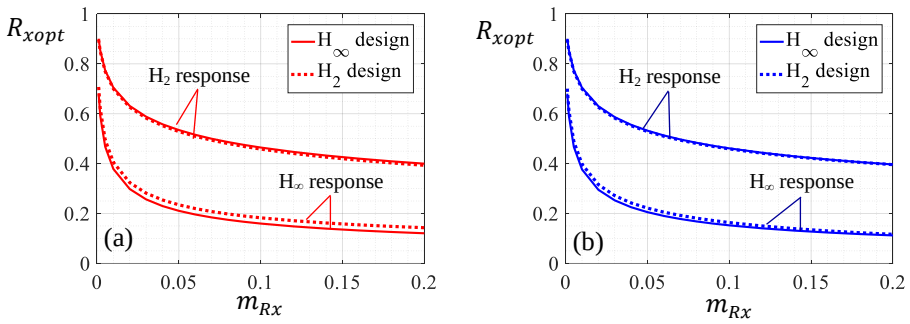

Figure 5. H_∞ and H_2 response ratios for the V-BTMD (left) and the H-BTMD (right) optimized according to either the H_∞ criterion or the H_2 criterion, as a function of m_{Rx} for ζ_{sx} = 2%.

3.2 The 3D first-order reconciliation

While the first stage of the procedure provides the dimensionless parameters of the BTMD which separately optimize its first-order 2D response along x and y, the second stage derives its corresponding physical parameters. This derivation, which is exact and univocal for the V-BTMD and the HT-BTMD, generally requires, for the HA-BTMD, an adjustment of the optimal dimensionless parameters obtained in the previous stage, to reconcile them with the constraints inherent in the spatial geometry of the device.

In fact, while for the V-BTMD the condition $\zeta_{xopt} = \zeta_{yopt}$ is satisfied by adopting distinct dampers along x and y, and for the HT-BTMD the condition $\mu_{0xopt} = \mu_{0yopt}$ is satisfied by adopting $\mu_0 = \mu_{0opt}$ in Eq. (4), for the HA-BTMD the condition $\chi_{xopt} = \chi_{yopt}$ is incompatible with the definition of χ_x and χ_y given by Eq. (29) and by its analogue expression in the y direction, except if $L_x = L_y$ (axial-symmetry) or $l_{p0} \to \infty$. In all other cases, at least one between χ_x and χ_y cannot be optimal. To minimize the distance of χ_x and χ_y from χ_{opt}, the position is therefore made that $\chi_{opt} = \sqrt{\chi_x \chi_y}$ which, recalling that $L_x \leq L_y$, results in the following expressions for χ_x and χ_y:

$$\chi_x = \chi_{opt}\sqrt{\frac{1+L_x/l_{p0}}{1+L_y/l_{p0}}} \leq \chi_{opt} \qquad \text{and} \qquad \chi_y = \chi_{opt}\sqrt{\frac{1+L_y/l_{p0}}{1+L_x/l_{p0}}} \geq \chi_{opt} \tag{35}$$

and in the following expression for the slip force:

$$p = mg\frac{\chi_{opt}}{\sqrt{(1+L_x/l_{p0})(1+L_y/l_{p0})}} \tag{36}$$

If $L_x = L_y$ or $l_{p0} \to \infty$, Eq. (36) ensures the HA-BTMD, both along x and y, the same 2D response as the optimal HT-BTMD. In all other cases, Eq. (36) makes the HA-BTMD suboptimal in both directions, namely underdamped along x and overdamped along y, to an extent which increases with the ratio L_y/L_x and decreases with l_{p0}. In all cases, l_{p0} appears an independent design parameter for the HA-BTMD, always affecting its first-order response.

In conclusion, once the optimal dimensionless parameters ω_{Ropt}, ζ_{opt}, χ_{opt} and μ_{0opt} are known, they can be used, together with m_R, l_{p0} and all the relevant structural parameters, to determine all BTMD dimensional parameters involved in the first-order model, i.e.: the BTMD mass ($m = m_R m_s$); the pendulum frequencies ($\omega_x = \omega_{Ropt}\omega_{sx}$ and $\omega_y = \omega_{Ropt}\omega_{sy}$) and lengths ($L_x = g/\omega_x^2$ and $L_y = g/\omega_y^2$); the damping coefficients for the V-BTMD ($c_x = 2\zeta_{opt}\omega_x m$ and $c_y = 2\zeta_{opt}\omega_y m$, if one damper is supposed in each direction); the slip force for the HA-BTMD (p according to Eq. (36)); and the friction pattern for the HT-BTMD ($\mu = \mu_{0opt}\|\nabla w\|$). The remaining BTMD parameters, involved beyond the range of small displacements, are instead determined as explained in Section 3.3 next.

3.3 The 3D design completion

The third stage of the procedure is the 3D design completion, meant to provide the BTMD parameters which, affecting the response of the absorber only in the large-displacement domain, are excluded from the previous stages. These parameters include the shape of the pendulum surface far from the origin, the length of the viscous dampers and the bumper characteristics. They also include the friction pattern far from the origin, unless already determined by a friction pattern law. Although these parameters too could be the object of a specific optimization based on the fully nonlinear model, they are left here to the free choice of the designer. This section offers possible guidelines for their selection.

3.3.1 The pendulum shape

The optimal pendulum lengths derived in Section 3.2 completely define the pendulum surface locally around the origin. Away from it, instead, distinct surfaces may correspond to the same L_x and L_y pair. For an ellipsoid of equation $w(u,v) = b_z\left(1 - \sqrt{1 - u^2/b_x^2 - v^2/b_y^2}\right)$, e.g., there are ∞^1 ways of choosing the semi-axes b_x, b_y and b_z to obtain the desired L_x and L_y, according to the relations $\frac{1}{L_x} = \left.\frac{\partial^2 w}{\partial u^2}\right|_{\mathbf{0}} = \frac{b_z}{b_x^2}$ and $\frac{1}{L_y} = \left.\frac{\partial^2 w}{\partial v^2}\right|_{\mathbf{0}} = \frac{b_z}{b_y^2}$. In this case the designer could freely impose, for instance, the further condition $b_z = \sqrt{b_x b_y}$ (leading to a spherical pendulum if $L_x = L_y$), in order to uniquely determine the ellipsoidal axes as follows: $b_x = \sqrt[4]{L_x^3 L_y}$, $b_y = \sqrt[4]{L_x L_y^3}$ and $b_z = \sqrt{L_x L_y}$. Alternative shapes could obviously be preferred, including for example the torus or the elliptic paraboloid. The search for the best option is here left for future work, and the ellipsoidal shape with $b_z = \sqrt{b_x b_y}$ will be adopted in all the following simulations.

3.3.2 The friction pattern

Similarly, the optimal friction pattern derived in Section 3.1 completely defines the friction coefficient only locally around the origin. Eqs. (4) and (22) are two of the infinite alternatives to extend it elsewhere. If an ellipsoidal pendulum is chosen and if Eq. (4) is adopted, the entire friction pattern is described by [13]:

$$\mu(\mathbf{q}) = \mu_0 \sqrt{\left(\frac{u^2}{L_x^2} + \frac{v^2}{L_y^2}\right) \Big/ \left(1 - \frac{u^2}{b_x^2} - \frac{v^2}{b_y^2}\right)} = \mu_0 \, \|\mathbf{H}_w \mathbf{q}\| / [1 - w(\mathbf{q})/b_z] \tag{37}$$

It can be easily shown [13] that:

- around the origin: $\mu(\mathbf{q}) \approx \mu_0 \|\mathbf{H}_w \mathbf{q}\| \to 0$;
- at the ellipsoid equator: $\mu(\mathbf{q}) \to \infty$;
- elsewhere: the iso-friction lines $\mu(\mathbf{q}) = \bar{\mu}$ and the level curves $w(\mathbf{q}) = \bar{w}$ coincide if $L_x = L_y$, otherwise they intersect along the surface as shown in Figure 6, where an ellipsoid is drawn having $L_y = 2L_x$ (and so $b_x \cong 1.19L_x$, $b_y \cong 1.68L_x$ and $b_z = \sqrt{2}L_x$), truncated at $w_{max} = b_z/2 = L_x/\sqrt{2}$. In the axonometric view, the z dimension is doubled for clarity. Both figures show 11 level curves, uniformly spaced between 0 and w_{max} and 11 iso-friction lines, uniformly spaced between 0 and $2\mu_0$.

(a)

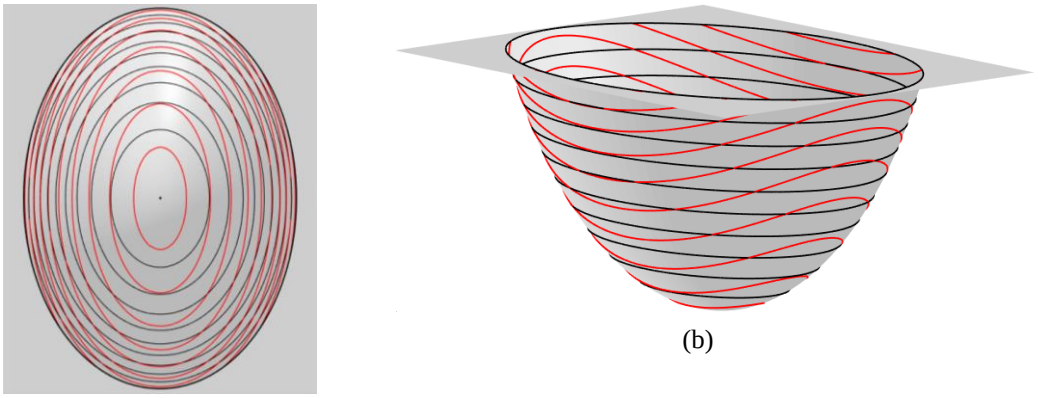

(b)

Figure 6. Intersection of level curves (black) and iso-friction lines (red) for $L_y/L_x = 2$: (a) xy view; (b) axonometric view (the z dimension being doubled for the sake of clarity).

3.3.3 Number and length of the viscous dampers

The optimal values of c_x and c_y are obtained in Section 3.2 by assuming a single damper in each horizontal direction. If more dampers are deployed in each direction, the corresponding coefficient must be subdivided among them. The length of the dampers is excluded from optimization and shall be chosen by the designer as appropriate, considering that the sensitivity of the damper to second-order effects decreases with its length. In all simulations, two dampers will be assumed henceforth in each direction, symmetrically disposed around the z axis, and the same length $l_{c0j} = \sqrt{L_x L_y} = b_z$ will be assigned to all dampers, with $j = 1{:}\,4$.

3.3.4 The bumper

The bumper is excluded from optimization too. Its stiffness and damping coefficient will be assigned to simulate a relatively rigid inelastic impact. Stiffness is taken as $k_r = m\omega_r^2$, with $\omega_r = 20\sqrt{\omega_x \omega_y}$ [21]. Damping is taken as $c_r = 2\zeta_r \omega_r m$, where $\zeta_r = -\frac{\ln e_r}{\sqrt{\pi^2 + \ln^2 e_r}}$ and e_r is the elastic restitution coefficient [22]. Assuming here $e_r = 0.5$, it follows that $\zeta_r = 0.2155$. Finally, clearance is taken as $w_r = b_z/2$.

4. Simulations in the small-displacement domain

In this section, the V-BTMD, HA-BTMD and HT-BTMD are compared in the small-displacement domain. In all cases, the BTMD is assumed to be designed according to the H_∞ criterion exposed in Section 3.1, here preferred because of its greater robustness. First 2D models and then 3D models are simulated under white-noise force input. In all cases, the structure is modelled as a 2%-damped SDOF system in each active horizontal direction.

4.1 2D models

The simplified first-order 2D model expressed by Eq. (28) is adopted. Optimization is conducted for the three BTMD types according to Sections 3.1 and 3.2, based on the H_∞ design criterion. Assuming for simplicity $L_x = L_y$, Eq. (35) implies for the HA-BTMD that $\chi_x = \chi_{opt}$, i.e. that the optimal HA-BTMD and HT-BTMD are equivalent and can be jointly referred to as the H-BTMD. With their optimal parameters selected according to Table 1, the V-BTMD and the H-BTMD are here evaluated by computing the system response to a stationary Gaussian zero-mean white-noise input process. As in Section 3.1, the stationary rms response is obtained through either solving the Lyapunov equation or performing Monte Carlo simulations, depending whether the system is linear or nonlinear. In the case of Monte Carlo simulations, 100 realizations are considered, assuming $t_{tot} = 3600T_{sx}$ and $t_s = 0.01T_{sx}$. By introducing the instantaneous power dissipated by the main structure as $W_s = \dot{\boldsymbol{q}}_s^T \mathbf{C}_s \dot{\mathbf{q}}_s = c_{sx}\dot{u}_s^2 + c_{sy}\dot{v}_s^2$,

three structural response quantities are used to measure the control performance, namely the rms structural displacement $u_{s,rms}$ (indeed corresponding to the H_2 norm of the transfer function $T_{u_s\bar{f}_{sx}}(\omega)$), the rms absorber stroke u_{rms}, and the mean structural dissipated power $W_{s,mean}$. Dividing the controlled by the uncontrolled values of the said three responses, the following three response ratios are obtained, adopted as performance indices: $R_{dx} = u_{s,rms}^{con}/u_{s,rms}^{unc}$ (indeed corresponding to the H_2 response ratio R_x adopted in Section 3.1), $R_{sx} = u_{rms}^{con}/u_{rms}^{unc}$ and $R_W = W_{s,mean}^{con}/W_{s,mean}^{unc}$.
For the V-BTMD and the H-BTMD, R_{dx}, R_{sx} and R_W are reported in Figure 7 for m_{Rx} ranging from 1‰ to 20%. The response ratios are nearly the same for the two types, with R_{dx} and R_W slightly smaller for the H-BTMD and R_{sx} slightly smaller for the V-BTMD. This result confirms the substantial equivalence of the V-BTMD and the H-BTMD in the presence of white noise input.

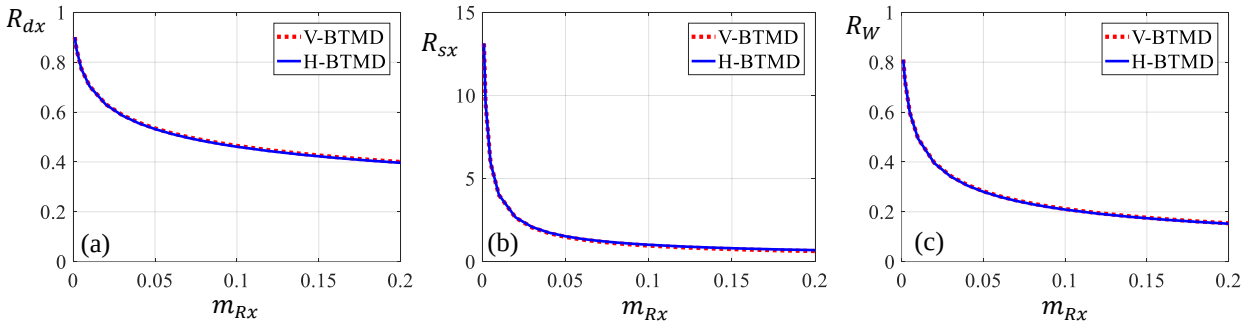

Figure 7. First-order 2D model under white-noise force input. Response ratios as a function of m_{Rx}.

4.2 3D models

The H_2 bidirectional performance of the three BTMD types, designed according to Sections 3.1. and 3.2 based on the H_∞ criterion, is here assessed by adopting the first-order 3D model of Eq. (26), with the input components f_{sx} and f_{sy} described as two independent stationary Gaussian zero-mean white-noise excitations, having rms values f_{sx0} and f_{sy0}, duration t_{tot} and sampling time t_s. Based on this model, the equations of motion along x and y are still linear and uncoupled for the V-BTMD but nonlinear and coupled for the HA-BTMD and the HT-BTMD.

4.2.1 Introductory example

As a preliminary step towards the assessment of the bidirectional performance of BTMDs, the case is first examined of an H_∞-optimal BTMD having m_R = 3% (the subscript x being here removed because $m_{Rx} = m_{Ry} = m_R$), mounted on a structure having mass m_s = 1 kg and natural periods $T_{sx} = T_{sy}$ (axial-symmetry). Because $T_{sx} = T_{sy}$ implies $L_x = L_y$ and therefore $\chi_x = \chi_y = \chi_{opt}$, the optimal HA-BTMD does not depend on l_{p0} (see again Eq. (35)) and, until a unidirectional excitation is considered, it performs exactly as the optimal HT-BTMD. If, instead, a bidirectional white-noise input is applied characterized by $f_{sx0} = f_{sy0} = 1$ N, $t_{tot} = 60$ s and $t_s = 0.01$ s, the response of the system in four possible configurations (no TMD, V-BTMD, HA-BTMD and HT-BTMD) is shown in Figure 8, where the following additional response quantities have been introduced: $W = \dot{\boldsymbol{r}}^T\mathbf{f}_d$, representing the instantaneous power dissipated by the BTMD; $W_{tot} = W_s + W$, representing the total instantaneous power dissipated by the overall system; $E_s(t) = \int_0^t W_s(\tau)d\tau$, $E(t) = \int_0^t W(\tau)d\tau$ and $E_{tot}(t) = \int_0^t W_{tot}(\tau)d\tau$, representing the energy dissipated until time t by, respectively, the structure, the BTMD and the overall system.
Figures 8 depicts the main features of the three BTMD types. Figures 8a to 8f compare the four configurations in terms of response time-histories and trajectories, the black curves referring to the uncontrolled structure, the red, green and blue curves to the structure equipped with, respectively, the V-

BTMD, the HA-BTMD and the HT-BTMD. Figures 8g to 8i, focused on the absorber dissipative behaviour during the last 20 seconds of simulation, report the planar view of the BTMD trajectories, discretized at every sample instant by monochrome circles of different intensities, the intensity being proportional to the power dissipated by the absorber at that instant, with a null intensity (white circle) corresponding to a null power and with a maximum intensity (black circle) corresponding to the maximum instantaneous power dissipated by the three BTMDs during those 20 seconds.

Two fundamental results are expressed by Figure 8.

The first result is that the V-BTMD and the HT-BTMD present a similar satisfactory bidirectional performance. In particular: (i) the structural displacements (Figures 8a and 8c) and the absorber strokes (Figures 8b and 8d) are similar for the two types; (ii) the absorber dissipated power, although exhibiting larger excursions in the case of the V-BTMD, present a similar mean trend, finally resulting in similar cumulative dissipated energy curves (Figure 8e and 8f); (iii) the "dissipative trajectories" shown in Figures 8g and 8i, although reflecting the different features of the two dissipative models (dissipation tends to increase with the absorber velocity for the V-BTMD and with the absorber stroke for the HT-BTMD), appear on the whole quite similar to each other.

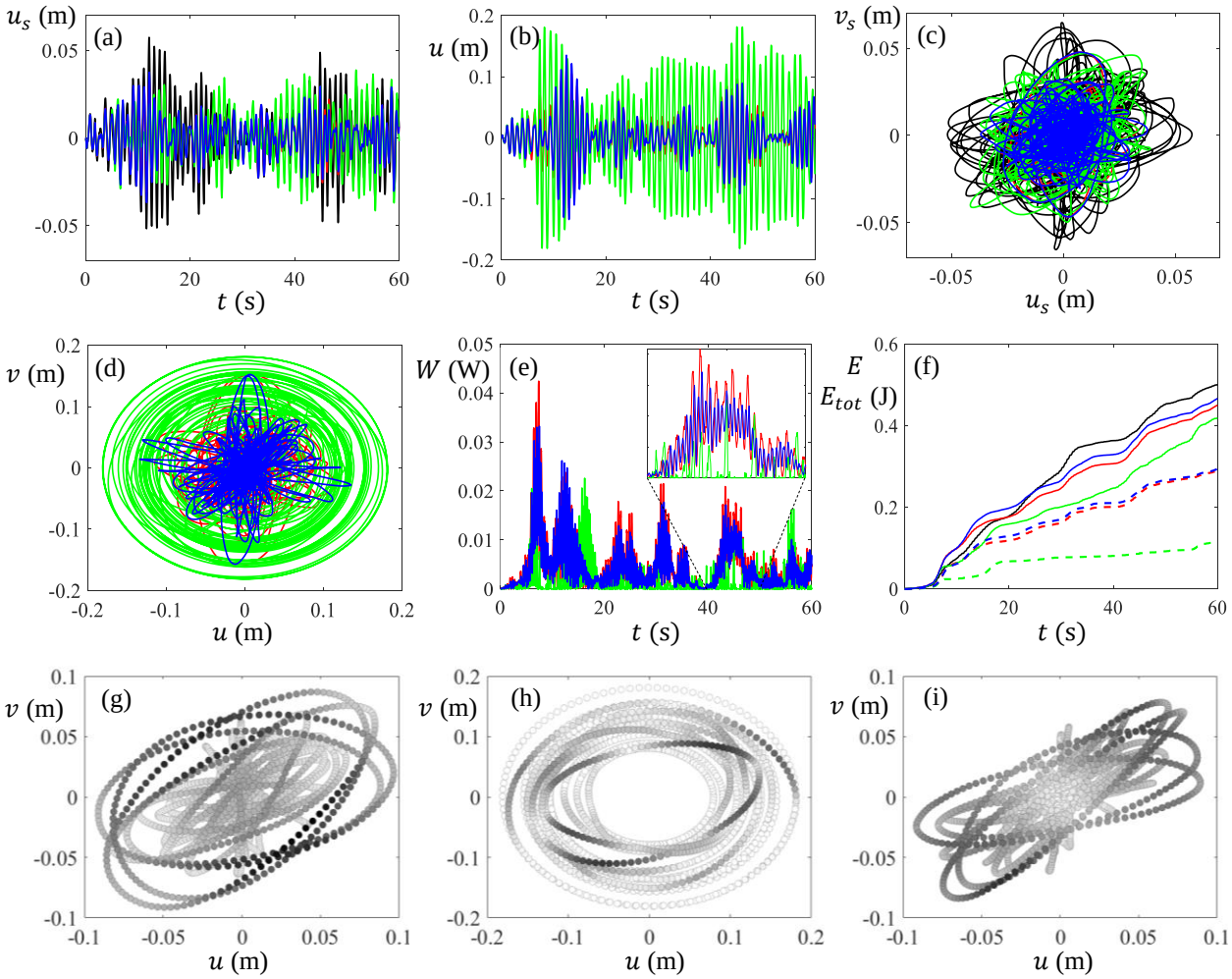

Figure 8. First-order 3D model under bidirectional white-noise force input. Response time-histories and trajectories for $T_{sx} = T_{sy} = 1.0$ s and $m_R = 3\%$. Figures (a) to (f): black = uncontrolled; red = V-BTMD; green = HA-BTMD; blue = HT-BTMD. Figure (f): dashed = E; continuous = E_{tot}. Figures (g) to (i): W increasing from white to black.

The second result, new to the best of the author's knowledge, is that the response of the HA-BTMD drastically diverges from the response of the other two types, soon after an initial transient period. The reason for this divergence clearly emerges from the HA-BTMD trajectories reported in Figures 8d and 8h, which appear as wide, nearly circular, scarcely-dissipative loops. The same damping impairment is visible in Figure 8e, where long time intervals are seen where the HA-BTMD dissipated power is nearly absent. Evidently, partly constrained by the radial arrangement of the axial-friction damper and partly encouraged by the axial-symmetry of the pendulum surface and by the equal value of the two horizontal force components, the motion of the HA-BTMD evolves through a series of virtually undamped revolutions around the z axis (non-dissipative because accompanied by no elongation of the friction damper), separated by non-circular, non-horizontal, pseudo-rotational loops, where a certain amount of energy dissipation is allowed by the damper elongation. By looking back at Eq. (21), which provides the first-order approximation of the friction damper axial elongation rate, it can be easily recognized that undamped loops are all those which, described by the equation $h_{px}u\dot{u} + h_{py}v\dot{v} = 0$, annul the axial elongation $\dot{s}_p$ of the damper, thus inhibiting its damping capability. The final result is that the equivalent damping ratio of the HA-BTMD drops, its stroke increases and its control effectiveness gets largely reduced (Figures 8a and 8f).

4.2.2 Generalization

The previous example is here generalized as follows: (i) the mass ratio m_R is alternatively set at 1%, 3% and 10%; (ii) keeping $T_{sx} = 1$ s, the ratio T_{sy}/T_{sx} between the two structural periods is ranged from 1 to 2; (iii) for any $T_{sy}/T_{sx} \neq 1$, because of the lost axial-symmetry, χ_x and χ_y now depend on l_{p0}, which is alternatively set at 0, $\sqrt{L_x L_y}$ or ∞ for comparison; (iv) the rms and mean responses are averaged over 100 realizations of the stochastic input process, each realization having duration $t_{tot} = 600$ s.

Results are reported in Figure 9 in terms of the following H_2 response ratios: $R_d = \sqrt{R_{dx}R_{dy}}$, $R_s = \sqrt{R_{sx}R_{sy}}$ and R_W, where R_{dx}, R_{sx} and R_W are defined as in Section 4.1, and R_{dy} and R_{sy} are the analogue of R_{dx} and R_{sx} in the y direction. It appears that: (i) the V-BTMD response ratios are constant with T_{sy}/T_{sx}; (ii) the HT-BTMD response ratios are approximately constant and nearly equal to the V-BTMD response ratios; (iii) the performance degradation of the HA-BTMD (revealed by an increase in both the structural response and the TMD stroke), confirmed for all mass ratios, strongly depends on T_{sy}/T_{sx}, being maximum in the axial-symmetrical case and diminishing as T_{sy}/T_{sx} increases, less rapidly as m_R gets larger; (iv) results for the HA-BTMD are slightly influenced by l_{p0}; the intermediate value, $l_{p0} = \sqrt{L_x L_y}$, achieves the best trade-off among the three response ratios, and will be therefore constantly adopted in the remaining of this paper.

To investigate how the response of the BTMD, and particularly of the HA-BTMD, depends on the relative amplitude of the two horizontal force components, the same simulations are repeated for different values of their respective ratio f_{sy0}/f_{sx0}. Results are reported in Figure 10 for m_R= 3%, omitting R_s for brevity. R_d and R_W appear independent from f_{sy0}/f_{sx0} for the V-BTMD, and nearly independent for the HT-BTMD. For the HA-BTMD, instead, f_{sy0}/f_{sx0} scarcely affects R_W but strongly influences R_d, which largely increases (even beyond the unit value which corresponds to the uncontrolled case) as f_{sy0}/f_{sx0} moves away from 1. This is evidently the result of the coupling effect induced by the above-mentioned undamped rotational motion of the HA-BTMD, which may increase the structural response in the less excited direction well beyond the uncontrolled value.

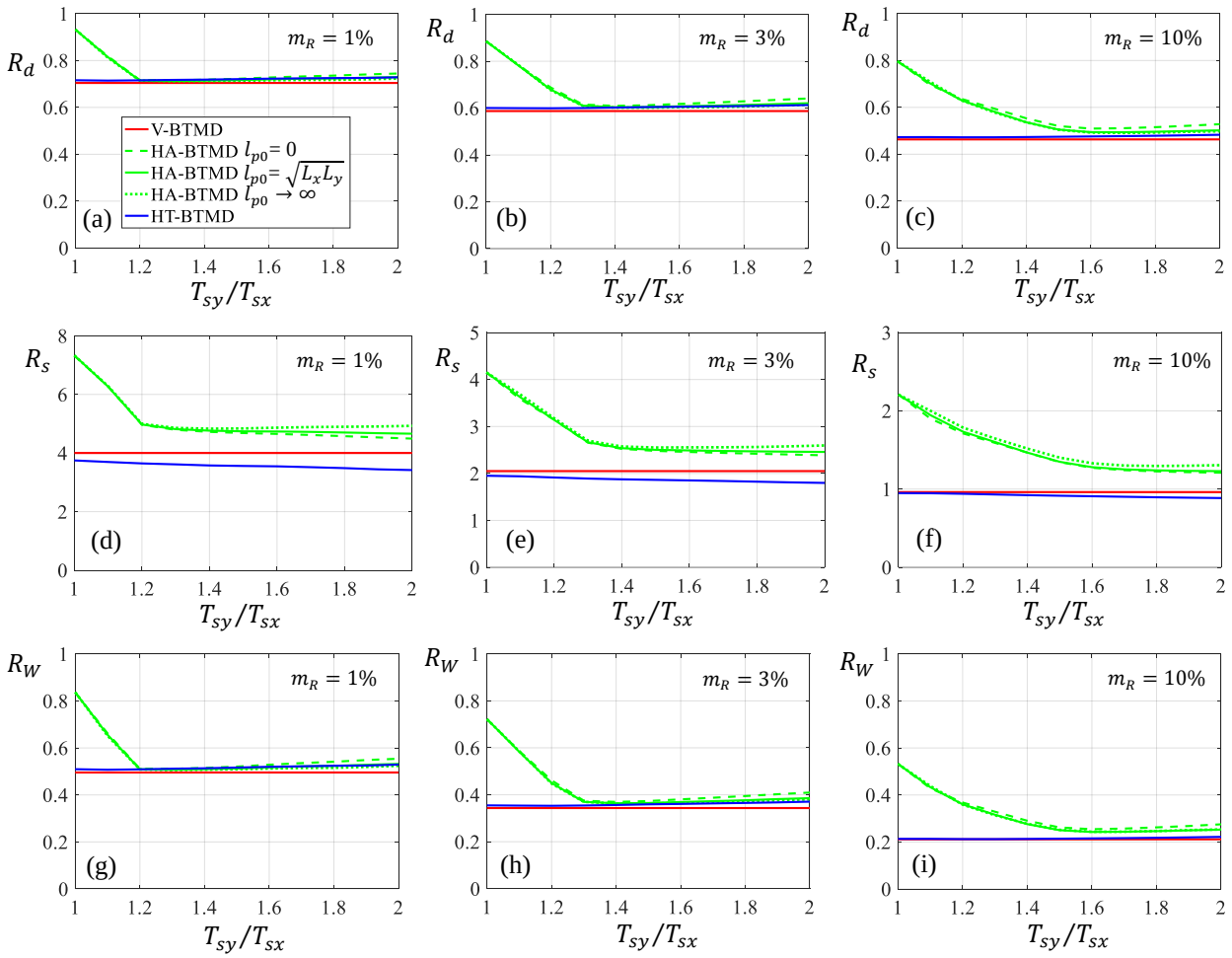

Figure 9. First-order 3D model under white-noise force input. Response ratios as a function of T_{sy}/T_{sx} for m_R = 1%, 3% and 10%.

5. Simulations in the large-displacement domain

This section extends the results of Section 4 to the large-displacement domain, to show the dependence of the BTMD behaviour on the excitation amplitude. Again, the H_∞-optimal BTMD is evaluated under white-noise force excitation.

5.1 2D models

Based on the fully nonlinear model expressed by Eq. (14), a 2%-damped SDOF structure having m_{sx} = 1 kg and T_{sx} = 1 s, equipped with an H_∞-optimal BTMD having m_{Rx} = 3%, is here observed under a unidirectional white-noise force input having rms amplitude f_{sx0}, duration t_{tot} = 600 s and sampling time t_s = 0.01 s. Because under large values of f_{sx0} the BTMD motion occurs in the large-displacement domain, simulations involve here other BTMD parameters than the few strictly necessary in first-order simulations. These other parameters, which for the present 2D problem include the pendulum shape, the friction pattern far from the origin, the length of the x-oriented viscous damper and the bumper characteristics, are here taken as suggested in Section 3.3, assuming for simplicity $L_y = L_x$.

Under these assumptions, the resulting H_2 response ratios R_{dx}, R_{sx} and R_W are reported in Figure 11 as a function of f_{sx0} ranging from 0 to 5 N.

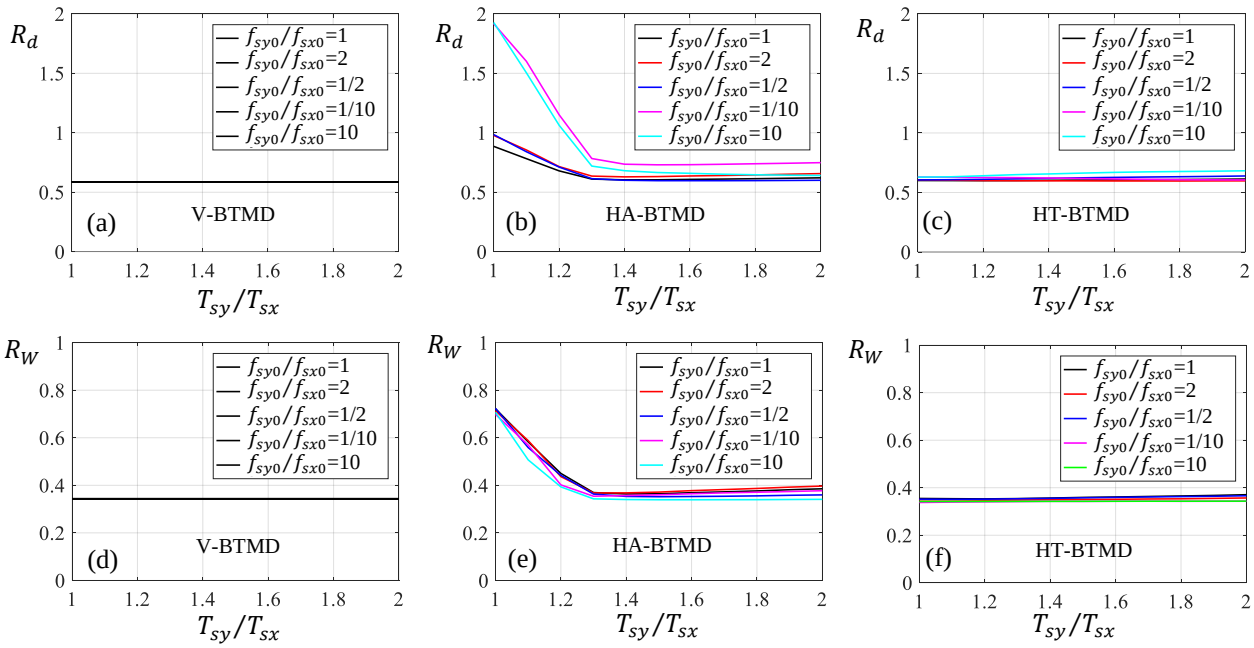

Figure 10. First-order 3D model under white-noise force input. Response ratios as a function of T_{sy}/T_{sx} for m_R = 3% and for different values of f_{sy0}/f_{sx0}.

For f_{sx0} = 0, Figure 11 confirms the first-order results obtained in Section 4.1. As f_{sx0} increases, however, as typical of pendulum absorbers [11], the control effectiveness worsens (R_{dx} and R_W increase) and the BTMD stroke decreases because of bumping and mistuning, for all BTMD types. The control loss appears similar for the V-BTMD and the HA-BTMD, and reduced (or delayed) for the HT-BTMD. This superior robustness of the HT-BTMD resides in the amplitude-increasing energy dissipation ensured by the gradient-proportional friction law, compared to the amplitude-decreasing equivalent damping provided by the viscous and the axial-friction dampers under large displacements.

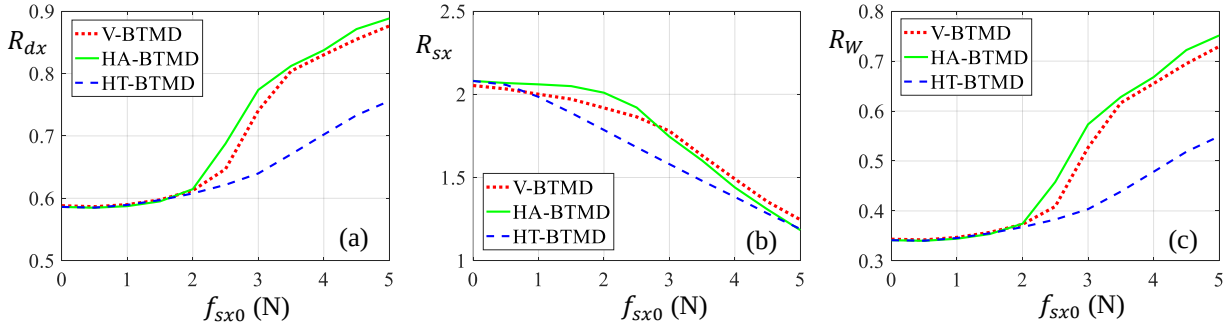

Figure 11. Fully nonlinear 2D model under white-noise force input. Response ratios as a function of f_{sx0} for m_R= 3%.

5.2 3D models

The problem described in Section 5.1 is here generalized to the case of a bidirectional force input having $f_{sx0} = f_{sy0}$. Keeping $T_{sx} = 1$ s, two values of T_{sy}/T_{sx} are considered, respectively equal to 1 and to 1.5. All other independent parameters are kept as in Section 5.1. Results are reported in Figure 12, which shows the H_2 response ratios R_d, R_s and R_W as a function of $f_{sx0} = f_{sy0}$, for the two chosen combinations of T_{sx} and T_{sy}. Figure 12 confirms the trends of performance loss already observed for the unidirectional

case in Figure 11, further aggravated for the HA-BTMD by the peculiar low-dissipative rotational behaviour of the axial-friction damper, already evident at small input amplitudes and particularly detrimental when $T_{sy}/T_{sx} = 1$ (axial-symmetry). Again, the HT-BTMD performs similarly to the V-BTMD for small amplitudes, and better for large ones.

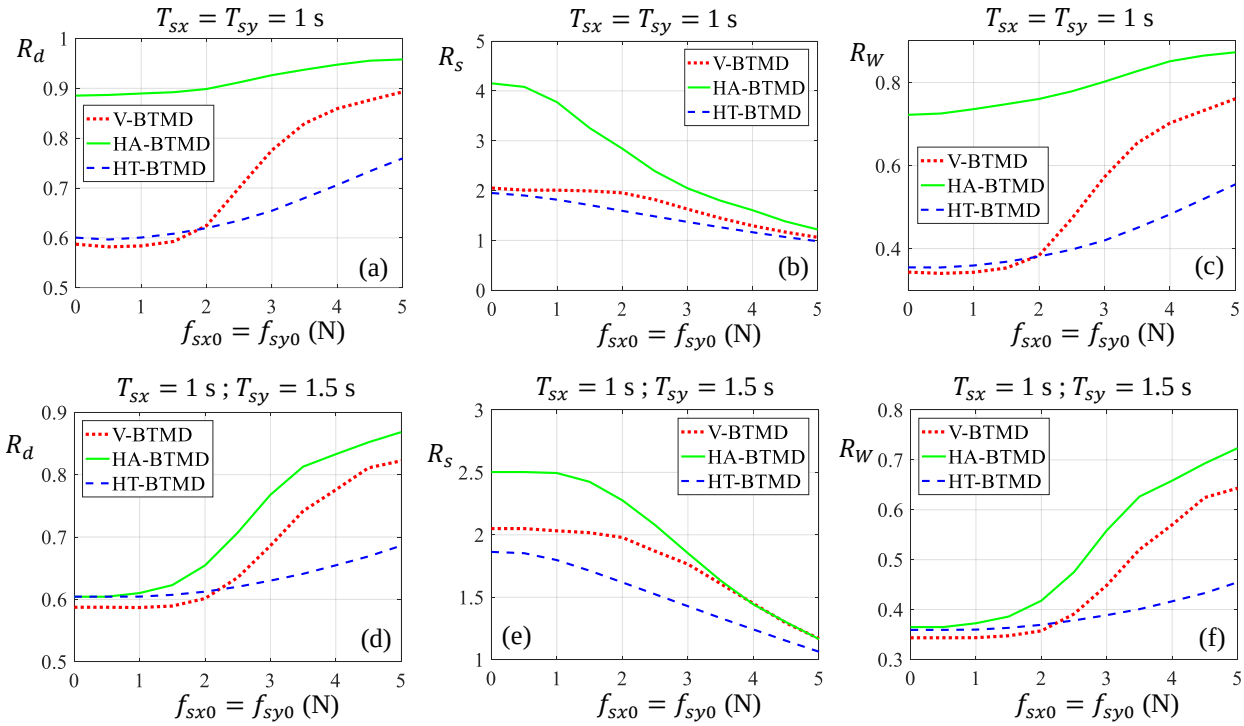

Figure 12. Fully nonlinear 3D model under white-noise force input. Response ratios as a function of $f_{sx0} = f_{sy0}$ for m_R= 3%. Figures a to c: $T_{sx} = T_{sy} = 1$ s; Figures d to f: $T_{sx} = 1$ s and $T_{sy} = 1.5$ s.

6. Case study: wind control of a high-rise building

In this section, an H_∞-optimal absorber of either V-, HA- or HT-BTMD types is simulated on an MDOF model of a high-rise building structure under wind excitation, based on the fully nonlinear model expressed by Eq. (14).

6.1 The structure

The structure is a 42-storey 168 m tall high-rise building, having constant 25 m x 25 m square section with 4.2 m chamfers at the corners. The building is modelled as a 10-elements tapered cantilever beam, with masses lumped at the nodes. The flexural stiffness is 1.21 times smaller along y than along x, resulting in natural periods 1.1 longer along y than along x. Main structural data are summarized in Table 3. The building shape, mass and stiffness are taken from [23], although scaled to increase the structural sensitivity to the across-wind component. The first three modes along x have periods of 4.00 s, 1.23 s and 0.52 s and participating modal masses of 45.3%, 21.8% and 11.1%. The modes along y are identical, except that periods are increased 1.1 times. Not to overemphasize the effectiveness of the absorber, a 2% damping ratio is assumed in each mode, which can be regarded as an upper bound for high-rise buildings in operational conditions [24].

Table 3. Main structural data of the 42-storey case-study building

Node number (-)	Height above the ground (m)	Mass ($kg \cdot 10^6$)	Flexural stiffness along x ($Nm^2 \cdot 10^{12}$)	Flexural stiffness along y ($Nm^2 \cdot 10^{12}$)	Tributary wind area (m^2)
1	21.4	3.54	55.90	46.20	515.0
2	41.2	3.13	33.00	27.27	495.0
3	61.0	2.96	21.60	17.85	468.8
4	78.7	2.73	13.80	11.40	442.5
5	96.4	2.43	7.85	6.49	442.5
6	114.1	2.00	4.03	3.33	387.5
7	127.4	1.51	1.69	1.40	332.5
8	140.7	1.60	1.03	0.85	332.5
9	154.0	1.45	0.55	0.45	341.3
10	168.0	1.34	0.22	0.18	175.0

6.2 The BTMD

The BTMD mass is taken as 1% the total mass of the building (m = 226900 kg). According to Warburton's classical approach [16], the corresponding 'effective' mass ratio is m_R = 6.45% in both horizontal directions. Interpolating from Table 1 with m_R = 6.45% provides the H_∞-optimal dimensionless parameters for the three absorber types. Table 4 reports such parameters in columns 2 to 5, and the corresponding main dimensional parameters in the following columns. It can be noticed that: (i) for the two H-BTMDs the dimensionless parameters and consequently the pendulum shape are (obviously) the same; (ii) the pendulum shape is narrower for the H-BTMDs than for the V-BTMD; (iii) the friction damping ratio μ_0 for the HT-BTMD, equal to 0.452, is sufficiently less than unity to ensure the re-centring capability of the device.

Table 4. Design parameters for the three BTMD types on the 42-storey building.

	ω_R (-)	ζ (-)	χ (-)	μ_0 (-)	T_x (s)	T_y (s)	L_x (m)	L_y (m)	b_x (m)	b_y (m)	b_z (m)	l_{c0j} (m)	l_{p0} (m)	w_r (m)
V-BTMD	0.932	0.154	-	-	4.29	4.72	4.57	5.53	4.79	5.27	5.03	5.03	-	2.51
HA-BTMD	0.982	-	0.452	-	4.07	4.48	4.12	4.99	4.32	4.76	4.53	-	4.53	2.27
HT-BTMD	0.982	-	-	0.452	4.07	4.48	4.12	4.99	4.32	4.76	4.53	-	-	2.27

6.3 The wind load

Simulations are conducted by subjecting the structure to a moderate-to-high wind flow, blowing for 1 hour either in the x direction or in the y direction. In either case, deterministic wind load time-histories are applied to the structural nodes, obtained as the realization of a stationary (in time) and nonhomogeneous (in space) stochastic process, including both along-wind and across-wind components, so as to excite the structure simultaneously in the two horizontal directions. Aeroelastic effects are neglected because irrelevant in the present case.

Along-wind loads are computed based on Davenport's along-wind load spectrum [25]. The one-sided drag force spectrum is taken as:

$$S_{F_iF_j}(\omega) = 24K_0\bar{W}_{10}^2C_d^2\left(\frac{z_iz_j}{100}\right)^{\alpha}A_iA_j coh\left(z_i, z_j, \omega\right)\frac{S_V(\omega)}{2\pi} \tag{38}$$

where the spanwise correlation function of the fluctuating force can be expressed as:

$$coh\left(z_i, z_j, \omega\right) = \exp\left(-\frac{C_1|\omega||z_i - z_j|}{2\pi\bar{V}_{10}}\right) \tag{39}$$

and the along-wind fluctuating wind velocity spectrum $S_V(\omega)$ can be expressed as:

$$S_V(\omega) = \frac{2t^2}{3f(1+t^2)^{4/3}} \tag{40}$$

in which $f = \omega/(2\pi)$ is the input frequency (expressed in Hz); $t = 1200\,f/\bar{V}_{10}$; $\bar{V}_{10}$ is the reference mean wind velocity at 10 m above the ground (expressed in m/s); $\bar{W}_{10} = 1/2\,\rho_a\bar{V}_{10}^2$ is the mean wind pressure at 10 m; ρ_a is the air density; K_0 is the surface drag coefficient; C_d is the drag coefficient; α is

the exponent for the mean velocity profile power law; C_1 is a constant; z_i and z_j are the heights of the *i*-th and *j*-th storey mass above the ground respectively; A_i and A_j are the tributary areas of the *i*-th and *j*-th mass respectively.

Across-wind loads are computed based on the spectrum proposed by Vickery and Clarke [26]. The one-sided across-wind spectrum is expressed as:

$$S_{F_iF_j}(\omega) = \frac{(\rho_a C_l \bar{V}_i \bar{V}_j)^2 A_i A_j}{8\pi^{1.5} B_s \sqrt{f_{s_i} f_{s_j}}} \cos(\alpha_1 R) \exp[-(R/\alpha_2)^2] \sqrt{\exp\left[-\frac{\left(1-f/f_{s_i}\right)^2 + \left(1-f/f_{s_j}\right)^2}{B_s^2}\right]} \qquad (41)$$

where $\cos(\alpha_1 R)\exp[-(R/\alpha_2)^2]$ is the spanwise correlation function of the across-wind wake excitation; $R = 2\left|z_i - z_j\right| / \left(D_i + D_j\right)$; α_1 and α_2 are non-dimensional coefficients pertaining to the correlation length; D_i and D_j are the sides of the square section at the heights z_i and z_j respectively; $\bar{V}_i = \bar{V}_{10}(z_i/10)^{\alpha}$ and $\bar{V}_j = \bar{V}_{10}\left(z_j/10\right)^{\alpha}$ are the mean wind velocities at z_i and z_j respectively; C_l is the lift coefficient; B_s is a measure of the relative width of the spectral peak; $f_{s_i} = S\bar{V}_i/D_i$ and $f_{s_j} = S\bar{V}_j/D_j$ are the vortex shedding frequency at z_i and z_j respectively; S is the Strouhal number.

Assuming the fluctuating wind velocity as a Gaussian process, the synthesis formula of the fluctuating wind load at point *i* is given as follows [27]:

$$F_i(t) = \sum_{j=1}^{i} \sum_{k=1}^{N_s} \left|\Gamma_{ij}(\omega_k)\right| \sqrt{2\Delta\omega_k} \cos\left(\omega_k t + \varphi_{jk}\right), \quad i = 1, 2, \ldots, N \qquad (42)$$

in which $H_{ij}(\omega_k)$ is the non-zero component of a lower triangular matrix $\mathbf{\Gamma}(\omega)$, obtained by decomposing the stochastic cross-spectrum matrices in Eqs. (38) and (41) using Cholesky's method; N is the number of lumped masses; $\Delta\omega_k$ is the frequency interval; $\omega_k = (k-1)\Delta\omega_k$; N_s is the number of frequency intervals; φ_{jk} is an independent random phase angle uniformly distributed between 0 and 2π.

In this example, the aerodynamic data pertaining to along-wind excitation are taken as follows [23]: $\bar{V}_{10}$ = 25.0 m/s; α = 0.25; C_d = 1.2; ρ_a = 1.23 kg/m^3; C_1 = 7.0; K_0 = 0.01; those pertaining to cross-wind excitation are as follows [27]: C_l = 0.40; S = 0.12; B_s = 0.26; α_1 = 0.5; α_2 = 5.0. With such data, the along- and across-wind spectra are obtained from Eqs. (38) and (39), and then deterministic time-histories of along and across wind-loads are simulated according to Eq. (42), for each structural node and for the duration of 1 hour. In Eq. (42), $\Delta\omega_k$ = 0.01 rad/s; $N_s = 2^{11}$; ω_{N_s} = 20.47 rad/s.

6.4 Results

Results are reported in Tables 5 to 8. Tables 5 and 6 refer to the wind blowing in the x direction, Tables 7 and 8 to the wind blowing in the y direction. In each table, 7 configurations are compared, respectively corresponding to: (i) the uncontrolled structure; (ii) a bidirectional linear TMD; (iii) a V-BTMD; (iv) an HA-BTMD; (v) an HT-BTMD; (vi) an H-BTMD (equivalently of the HA- or of the HT- types) under the along-wind force component only; (vii) an H-BTMD under the across-wind force component only. Considering both along and across wind components, configurations (i) to (v) fully account for the bidirectional response of the structure-BTMD system. Considering only one wind component, configurations (vi) and (vii) account only for the 2D response of the structure-BTMD system, thus cancelling the friction-coupling effect. By comparing configurations (vi) and (vii) with configurations (iv) and (v), the influence of such coupling effect is assessed. For each configuration, several response quantities are reported in Tables 5 to 8 as a measure of the absorber performance. Denoting by u_{sN}, v_{sN} and r_{sN} respectively the x component, the y component and the modulus of the top storey displacement, by u, v and r respectively the x component, the y component and the modulus of the absorber stroke, by a_x, a_y and a_h respectively the x component, the y component and the modulus of the structural top storey acceleration, and by W_s the instantaneous power dissipated by the main structure, Tables 5 and 7 report the maximum (over time and in absolute value) structural displacement, the maximum TMD stroke, the maximum structural acceleration and the maximum friction damping ratio obtained during simulations, while Tables 6 and 8 report the rms structural displacement, the rms TMD stroke, the rms structural acceleration and the mean structural dissipated power.

Table 5. Wind blowing in the X direction – Maximum (in-time) responses

Configuration	$u_{sN,max}$ (cm)	$v_{sN,max}$ (cm)	$r_{sN,max}$ (cm)	u_{max} (cm)	v_{max} (cm)	r_{max} (cm)	$a_{x,max}$ (cm/s^2)	$a_{y,max}$ (cm/s^2)	$a_{h,max}$ (cm/s^2)	μ_{max} (-)
Uncontrolled	15.8	79.4	79.4	0.0	0.0	0.0	47.4	167	167	-
Linear TMD	11.4	39.1	39.6	18.7	110	110	32.1	84.5	84.8	-
V-BTMD	11.4	39.1	39.7	18.8	109	109	32.1	84.6	84.8	-
HA-BTMD	44.9	60.4	60.4	142	149	149	121	120	121	-
HT-BTMD	10.3	37.8	38.4	17.3	107	107	34.5	103	103	0.10
H-BTMD along	10.9	-	-	17.2	-	-	28.9	-	-	0.02
H-BTMD across	-	39.4	-	-	105	-	-	107	-	0.10

Table 6. Wind blowing in the X direction – RMS (in-time) responses and mean power dissipation

Configuration	$u_{sN,rms}$ (cm)	$v_{sN,rms}$ (cm)	$r_{sN,rms}$ (cm)	u_{rms} (cm)	v_{rms} (cm)	r_{rms} (cm)	$a_{x,rms}$ (cm/s^2)	$a_{y,rms}$ (cm/s^2)	$a_{h,rms}$ (cm/s^2)	$W_{s,mean}$ (kW)
Uncontrolled	5.0	26.8	27.3	0.0	0.0	0.0	13.3	55.2	56.8	31.1
Linear TMD	3.1	13.4	13.7	5.9	37.1	37.5	8.6	28.7	30.0	8.12
V-BTMD	3.1	13.4	13.8	6.0	36.9	37.4	8.6	28.8	30.1	8.17
HA-BTMD	11.8	16.7	20.5	45.2	49.5	67.0	25.5	34.1	42.5	17.4
HT-BTMD	3.4	13.3	13.7	5.0	37.4	37.8	9.0	30.6	31.9	8.63
H-BTMD along	3.1	-	-	6.0	-	-	8.8	-	-	-
H-BTMD across	-	13.5	-	-	35.9	-	-	31.3	-	-

Table 7. Wind blowing in the Y direction – Maximum (in-time) responses

Configuration	$u_{sN,max}$ (cm)	$v_{sN,max}$ (cm)	$r_{sN,max}$ (cm)	u_{max} (cm)	v_{max} (cm)	r_{max} (cm)	$a_{x,max}$ (cm/s^2)	$a_{y,max}$ (cm/s^2)	$a_{h,max}$ (cm/s^2)	μ_{max} (-)
Uncontrolled	73.8	18.0	74.0	0.0	0.0	0.0	176	45.6	177	-
Linear TMD	35.5	14.4	36.1	99.2	26.9	101	85.3	41.2	86.2	-
V-BTMD	35.5	14.4	36.1	98.8	26.8	101	85.3	40.9	86.1	-
HA-BTMD	49.0	49.9	53.3	134	140	140	116	96.6	129	-
HT-BTMD	36.2	17.6	36.9	98.6	22.4	99.3	91.9	45.9	92.8	0.11
H-BTMD along	-	14.8	-	-	25.0	-	-	41.6	-	0.02
H-BTMD across	36.5	-	-	99.9	-	-	91.6	-	-	0.11

Table 8. Wind blowing in the Y direction – RMS (in-time) responses

Configuration	$u_{sN,rms}$ (cm)	$v_{sN,rms}$ (cm)	$r_{sN,rms}$ (cm)	u_{rms} (cm)	v_{rms} (cm)	r_{rms} (cm)	$a_{x,rms}$ (cm/s^2)	$a_{y,rms}$ (cm/s^2)	$a_{h,rms}$ (cm/s^2)	$W_{s,mean}$ (kW)
Uncontrolled	26.7	6.0	27.3	0.0	0.0	0.0	65.3	13.3	66.6	40.2
Linear TMD	11.8	4.0	12.5	33.0	8.0	34.0	28.2	9.2	29.6	7.89
V-BTMD	11.9	4.0	12.5	33.0	8.0	33.9	28.3	9.2	29.8	7.96
HA-BTMD	14.6	16.0	21.6	48.3	45.3	66.2	34.0	30.8	45.9	20.3
HT-BTMD	11.9	4.4	12.6	33.3	6.1	33.8	29.5	10.0	31.1	8.41
H-BTMD along	-	4.0	-	-	7.6	-	-	9.5	-	-
H-BTMD across	11.8	-	-	33.3	-	-	29.6	-	-	-

6.5 Discussion

Results in Table 5 to 8 can be commented as follows:

1) For the uncontrolled structure, the response to the across wind component is around 4÷5 times prevalent. The maximum and the rms displacements are respectively around 0.8 m and 0.3 m.

2) The ideally linear TMD proves quite effective: both the max and the rms responses drop to about 50% (displacements and accelerations) and to 20÷25% (power). Effectiveness is maximum for the across-wind component (which induces on the structure a larger dynamic amplification), and almost the same for the wind blowing along x or y. The maximum and the rms TMD displacements are respectively around 1÷1.1 m and 0.35÷0.4 m.

3) The V-BTMD gives nearly identical results to the linear TMD. TMD strokes are relatively small and the bumper is far from being activated, so the first-order approximated model proves accurate.

4) The HA-BTMD exhibits, under bidirectional input, a substantial performance degradation with respect to all other configurations. A strong coupling occurs between the two directions, which may even increase the structural response beyond its uncontrolled value in the less excited direction (i.e. in the along-wind direction). With respect to the V-BTMD, structural displacements and accelerations increase on average by a factor of 1.5, W_s by a factor of 2.3 and TMD strokes by factors of 1.4 and 1.9, respectively in maximum and rms terms. This degradation does not completely annul the effectiveness of the absorber, but produces a structural response halfway between the uncontrolled one and the one obtained with the V-BTMD.

5) The HT-BTMD exhibits, under bidirectional input, a performance only very slightly reduced with respect to the V-BTMD: accelerations increase by about 10% and W_s by around 6%, but structural displacements and TMD strokes slightly decrease by about 1%. The maximum value of the tangential-friction coefficient met by the absorber during its motion is 0.11.

6) Both H-BTMD types exhibit, under unidirectional input, nearly the same overall performance of the V-BTMD: displacements are unvaried, TMD strokes decrease by about 3%, accelerations and W_s increase by about 5%. Comparing these results to those obtained for the HA-BTMD and the HT-BTMD under bidirectional motion confirms the little influence that friction coupling has for the HT-BTMD and the detrimental role it has instead for the HA-BTMD.

7) Depending on the adopted type of BTMD, the absorber maximum stroke approximately varies in the range 1÷1.5 m. Should a single concavity allowing for such strokes be considered impractically large, two concavities facing each other with a roller or a slider in between could be used instead, halving its size [11].

7. Conclusions

The main achievements of this study can be summarized as follows:

1) A unifying analytical model is established for simulating viscous (V-BTMD), axial-friction (HA-BTMD) and tangential-friction (HT-BTMD) BTMDs, rigorously accounting for their mechanical and geometrical nonlinearities. Its first-order reduction highlights the main properties of the three types, including some undocumented issues of fundamental practical importance, such as the control loss observable in symmetrical or nearly-symmetrical HA-BTMDs under bidirectional motion.
2) The H_∞ and the H_2 optimal design problems are rigorously posed and numerically solved for friction BTMDs on linear structures under harmonic or white-noise force excitations. Tables and figures providing the optimal BTMD parameters and the resulting control performance as a function of the BTMD mass ratio are presented that can be directly used as a practical design tool. The H_∞ design proves more robust than the H_2 design, in that the H_∞-designed device exhibits an H_2 performance only slightly less than optimal, whereas the H_2-designed device exhibits an H_∞ performance which may be much less than optimal. Compared with the exact optimal solution, the suboptimal solution proposed in previous studies, based on friction-to-viscous equivalence, proves only slightly less effective in reducing the H_2 structural response, but significantly less effective in reducing the H_∞ structural response, especially in the case of large mass ratios.

3) In 2D first-order problems, the HA-BTMD and the HT-BTMD are exactly equivalent, and if properly designed their effectiveness proves nearly the same as that of the V-BTMD, independently from the excitation level.
4) In 3D first-order problems, the performance of the V-BTMD remains unchanged and that of the HT-BTMD gets only slightly reduced by friction coupling. The HA-BTMD response, instead, becomes dramatically dependent on the pendulum shape: if the ratio between the two pendulum lengths is far from 1, the performance appears similar to that of the other two types; but as the ratio approaches 1, the control effectiveness diminishes and the TMD strokes increase because of the insurgence of a peculiar insufficiently-damped rotational mode of the HA-BTMD around the vertical axis.
5) If analyses are extended to the large-displacement domain, the main trends depicted above remain unchanged except that for all BTMD types the control performance progressively reduces as the excitation amplitude increases, because of bumping and mistuning; this reduction is smaller for the HT-BTMD because of the favourable features of the assumed friction law.

In conclusion, once properly designed and until stroke demand does not exceed their intrinsic stroke limitations, BTMDs appear an effective alternative to translational TMDs, applicable through a variety of damping options. The two homogeneous friction mechanisms, and particularly the tangential one, are promising novel paradigms to provide amplitude-independent damping to engineering pendular systems.

Acknowledgements
This research was kindly supported by Politecnico di Torino.

References

1. G.W. Housner, L.A. Bergman, T.K. Caughey et al., Structural control: past, present, and future, J. Eng. Mech. 123/9 (1997) 897–971.
2. M. Pirner, Actual behaviour of a ball vibration absorber, J.Wind Eng. Ind. Aerodyn. 90 (2002) 987–1005.
3. J. Náprstek, C. Fischer, M. Pirner, O. Fischer, Non-linear model of a ball vibration absorber, Comput. Meth. Applied Sciences 30 (2013) 381–396.
4. V.P. Legeza, Dynamics of vibroprotective systems with roller dampers of low-frequency vibrations, Strength Mat. 36/2 (2004) 185–194.
5. E. Matta, A. De Stefano, Robust design of mass-uncertain rolling pendulum TMDs for the seismic protection of buildings, Mech. Syst. Signal Proc. 23 (2009) 127–147.
6. J. Chen, C.T. Georgakis, Tuned rolling-ball dampers for vibration control in wind turbines, J. Sound Vibr. 332 (2013) 5271–5282.
7. M. Bransch, Unbalanced oil filled sphere as rolling pendulum on a flat surface to damp horizontal structural vibrations, J. Sound Vibr. 368 (2016) 22–35.
8. J. Wang, N.E. Wierschem, B.F. Spencer Jr., X. Lu, Experimental study of track nonlinear energy sinks for dynamic response reduction, Eng. Struct. 94 (2015) 9–15.
9. J. Wang, N.E. Wierschem, B.F. Spencer Jr., X. Lu, Numerical and experimental study of the performance of a single-sided vibro-impact track nonlinear energy sink, Earthq. Eng. Struct. Dyn. 45 (2016) 635–652.
10. S. Li, L. Fu, F. Kong, Seismic response reduction of structures equipped with a voided biaxial slab-based tuned rolling mass damper, Shock and Vibration 2015/760394 (2015) 1–15.
11. E. Matta, A. De Stefano, B.F. Spencer Jr., A new passive rolling-pendulum vibration absorber using a non-axial-symmetrical guide to achieve bidirectional tuning, Earthq. Eng. Struct. Dyn. 38 (2009) 1729–1750.
12. J.L. Almazan, J.C. De la Llera, J.A. Inaudi, D. Lopez-Garcia, L.E. Izquierdo, A Bidirectional and homogeneous tuned mass damper: a new device for passive control of vibrations, Eng. Struct. 29 (2007) 1548–1560.

13. E. Matta, A novel bidirectional pendulum tuned mass damper using spatially-variable homogeneous tangential friction to achieve amplitude-independent control effectiveness, submitted Jan. 2018 to Earth. Eng. Struct. Dyn.
14. J. Inaudi, J. Kelly, Mass damper using friction-dissipating devices, J. Eng. Mech. 121 (1995) 142–149.
15. F. Ricciardelli, B.J. Vickery, Tuned vibration absorbers with dry friction damping, Earthq. Eng. Struct. Dyn. 28/7 (1999) 707–723.
16. G.B. Warburton, Optimum absorber parameters for various combinations of response and excitation parameters, Earth. Eng. Struct. Dyn. 10 (1982) 381–401.
17. R. Greco, G.C. Marano, Optimum design of Tuned Mass Dampers by displacement, Soil Dyn. and Earthq. Eng. 49 (2013) 243–253.
18. S.V. Bakre, R.S. Jangid, Optimum parameters of tuned mass damper for damped main system, Struct. Control Health Monit. 14 (2007) 448–470.;
19. A.Y.T. Leung, H. Zhang, Particle swarm optimization of tuned mass dampers, Eng. Struct. 31 (2009) 715–728.
20. J.B. Burl, Linear Optimal Control, Addison-Wesley, Longman, Reading, MA, Menlo Park, CA, USA, 1999.
21. Z. Lu, Z. Wang, S.F. Masri, X. Lu, Particle impact dampers: past, present, and future, Struct. Control. Health Monit. e2058 (2017) 1–25.
22. J. Shäfer, S. Dippel, D. Wolf, Force schemes in simulations of granular materials, Journal de Physique I, EDP Sciences 6/1 (1996) 5–20.
23. Y.L. Xu, B. Samali, K.C.S. Kwok, Control of along-wind response of structures by mass and liquid dampers, J. Eng. Mech. 118/1 (1992) 20–39.
24. J.R. Wu, P.F. Liu, Q.S. Li, Effects of amplitude-dependent damping and time constant on wind-induced responses of super tall building, Comput. Struct. 85 (2007) 1165–1176.
25. A.G. Davenport, The spectrum of horizontal gustiness near the ground in high winds, Q. J. R. Meteorol. Soc. 87 (1961) 194–211.
26. B.J. Vickery, A.W. Clarke, Lift or across-wind response of tapered stacks, J. Struct. Div. ASCE 98 (1972) 1–20.
27. M. Shinozuka, G. Deodatis, Simulation of stochastic processes by spectral representation, J. Appl. Mech., 44/4 (1991) 191–204.